Stony Brook University

OFFICIAL COPY

The official electronic file of this thesis or dissertation is maintained by the University Libraries on behalf of The Graduate School at Stony Brook University.

© All Rights Reserved by Author.

Identification of Nonlinear Properties of Thermal Spray Zirconia under Mechanical Loading

A Thesis Presented

by

Xi Yang

to

The Graduate School

in Partial Fulfillment of the

Requirements

for the Degree of

Master of Science

in

Mechanical Engineering

Stony Brook University

August 2009

Stony Brook University

The Graduate School

Xi Yang

We, the thesis committee for the above candidate for the

Master of Science degree, hereby recommend

acceptance of this thesis.

Toshio Nakamura – Thesis Advisor
Professor – Department of Mechanical Engineering

Chad Korach – Chairperson of Defense
Assistant Professor – Department of Mechanical Engineering

Sanjay Sampath – Outside Member
Professor – Department of Materials Science and Engineering

This thesis is accepted by the Graduate School

Lawrence Martin
Dean of the Graduate School

Abstract of the Thesis

Identification of Nonlinear Properties of Thermal Spray Zirconia under Mechanical Loading

by

Xi Yang

Master of Science

In

Mechanical Engineering

Stony Brook University

2009

Thermal sprayed Yttria stabilized zirconia coatings exhibit nonlinear mechanical responses as the stresses within coating change. This behavior can be explained by the microstructure of the TS coating materials (pores, micro-cracks, splat boundaries etc.). A robust procedure to estimate the nonlinear properties of the TS coating by mechanical bending is introduced in this paper. The loading condition used in this study is generated by four-point-bend test. Compare to other loading condition, four-point-bend test can generate higher stress in TS coating, and also it takes short time to carry out and eliminates CTE effect, which makes it a suitable method to generate pure mechanical loading condition.

To estimate nonlinear properties of coating, first, a suitable stress-strain model is proposed to describe the nonlinear behavior, and a bi-material beam solution is derived. Then an inverse analysis is utilized to extract the unknown nonlinear parameters from the moment-curvature measurements. Prior to applying the procedure to process the actual specimens, a detailed verification study using finite element simulations was carried out to examine the accuracy and robustness of the method. Here, the sensitivities of the

measurement errors and calculation of each parameter are studies carefully. Also a comparison with the procedure based on thermal cycle test is discussed.

After the verification, actual moment-curvature measurements of TS YSZ coating are used to determine the nonlinear properties. According to the estimated results, HOSP and FC specimens have different mechanical responses under mechanical loading due to the different microstructure of the powders. Also different spraying approaches can result in the coatings behave different. A comparison of the coatings' behavior under four-point-bend test and thermal cycle test is presented at the end. The results show that TS coatings have stiffer mechanical response in mechanical loading condition than thermal loading.

To my parents and friends

For their supports

Table of Contents

List of Figures

List of Tables

Acknowledgements

The two years' study in pursuing a master degree is the best experience of my life. I am deeply grateful to my advisor, Professor Toshio Nakamura. His broad knowledge and passion toward scientific research encourage me to devote myself to the study of solid mechanics. He is not only a mentor on academics but also with a concern for the well being of his students. Besides my advisor, I also want to thank the rest of my thesis committee, Professor Chad Korach and Professor Sanjay Sampath, who gave me insightful comments and reviewed my work on a very shot of notice. Special thanks to Gopal Dwivedi from Department of Materials Science and Engineering, who did most of the four-point-bend tests and helped me process the data. I would also like to thank all the faculty and staff in the Department of Mechanical Engineering, for their help with my studies and financial support from NSF GOALI-FRG program under award CMMI 0605704.

I am indebted to my senior colleagues: Dr. Nanayanan Ramanujam, Jian Yao, Wei Zhao, for their generous help. I also want to thank all my fellow group colleagues: Chong Huang, Yu Chen, Shu Guo, and many others, for their care, support and friendship.

Last but not the least, I want to thank my parents, for their loving, supporting, concerning and understanding during my graduate study. This thesis is dedicated to them.

To all of you, thank you.

1. Introduction

Thermal sprayed (TS) coatings are extremely effective in increasing component life and value, decreasing machinery down-time, and improving performance in a wide variety of applications. Aerospace, automotive, biomedical, printing, paper making, oil and gas, electronics, and food processing equipment are just a few of the industries achieving new and better results with thermal spray coatings. As the engineering application increases, their mechanical reliability becomes more critical to ensure designed performances. The coating's properties, such as effective modulus, thermal conductivity and residual stresses, are key factors in understanding coating's reliability (Kesler et al., 1998).

Often TS ceramic coatings are synthesized with plasma spray guns where feedstock particles are melted at extreme temperatures. The molten or semi-molten splats solidify rapidly on substrate surfaces to form a coating. This process generates lamellar microstructure as well as many defects such as pores and cracks. This unique structure results in the nonlinear mechanical elastic behavior by the opening and closing of the micro-cracks and pores and sliding between splats interfaces under compressive and tensile load (Liu and Nakamura, 2006). Under high compressive load, crack faces are closed and the coatings exhibit higher apparent stiffness while opened cracks under tensile state produce more compliant response (Kroupa and Dubsky, 1999; Kroupa and Plesek, 2002). Many methods were carried out to exam the nonlinear properties of TS coating. Liu and Nakamura (2006) reported the nonlinear behavior of the thermal under thermal cycling test. Harok and Neufuss (2001) reported nonlinear behavior of atmospheric plasma sprayed (APS) $ZrSiO_4$ under four-point-bend tests. Waki et al. (2004) observed the nonlinear stress-strain responses of plasma sprayed zirconia coating using the laser speckle strain-displacement gauge (SSDG). Wang et al. (2006) showed nonlinear stress-strain relation of thermally sprayed metallic Ni–45Cr coating under tensile loading along the through-thickness direction due to its lamellar features.

The determination of the nonlinear property is important to evaluate effectiveness of the thermal spray coating. Liu and Nakamura (2006) provided an effective method to estimate the nonlinear properties of the TS coating under thermal cycling test; Eldridge,

Morscher and Choi (2002) measured the modulus of the coating using ultrasonic techniques; Basu, Funke, and Steinbrech (1999) and Steinbrech (2002) reported the stiffness of the TS coating under indentation tests; Kucuk, Berndt, Senturk, and Lima (2000) analyzed the coating behavior for different coating and substrate thickness and temperature under four point bending test.

Scholten, Dortmans and Bach (1992) first demonstrated that using bend or compressive/tensile loading, some properties of the beam can be determined. Even the determination of Young's modulus E the individual layers from the global data obtained in a test with a composite specimen is still limited and short of theoretical formulation (Kucuk, Berndt, Senturk, Lima, and Lima, 2000 and Kim and Nairn, 2000), an approximate bi-layer beam solution can be used to determine the modulus. Kroupa and Plesek observed the Young's modulus of coating will increase when coating is in compression. Nohava, Kroupa (2005) studied the variation of coating's Young's modulus in tension under four-point-bend test. In this paper, the mechanical stress is also generated by four-point-bend test. The nonlinear parameters in the proposed constitutive model are estimated using an inverse analysis to extract the best estimates of unknown material parameters from measured moment-curvature data.

2. Substrate–curvature measurements

2.1 Background

Four-point-bend test is an effective method to estimate properties of thin films and coatings. The measured data can be processed via either bimaterial or Stoney formula (if the material is very thin compared to the substrate) to determined the unknown properties. Using thermal tests, the substrate–curvature method based on Stoney formula has been also widely used in various applications (e.g., Carlotti et al., 1997; Lacquaniti et al., 1997; Krulevitch et al., 1996; Hunsche et al., 2001; Oka et al., 2003; Menzel et al., 2005; Kuroda et al. 1988, 1990). However, the limitation of Stoney formula method is that the thickness of the coating has to be very small compare to the thickness of the substrate. If the thickness of the coating is not that small, another method has to be introduced to solve the curvature relation. While if the total thickness of the beam is smaller than 10% of the length of the beam ($t/h \leq 1/10$), the beam theory can be used to solve the curvature equation.

There are many methods to measure curvature changes. Liu and Nakamura have built a perfect method to estimate unknown properties from curvature measurement under temperature change. Curvature measurement under temperature change is a well-established method and has been utilized to many applications (Liu and Nakamura, 2006). Compare to the temperature cycling test, curvature measurement under four-point-bend test offers some advantages that can be regarded as an alternated method to estimate the unknown properties. First, it takes a very short time (generally several minutes) to carry out four-point-bend test; however the thermal cycle test might take a few hours to complete the whole process. Second, thermal cycle test requires the CTE of substrate has to be much greater than the coating to generate curvature, while four-point-bend test does not constrained by the substrate material, which can be used to investigate coating properties on much more kinds of substrates. Thirdly, four-point-bend test can generate a higher stress in the coating (which can go up to 50–60MPa), however for the thermal cycle test, the maximum stress is generally smaller than 10MPa. Fourth, four-point-bend test is a pure mechanical loading test, which can estimate the coating's behavior without

temperature effect. And if carrying out the four-point-bend test in different temperature condition, it can test temperature influence to the coating's performance. However, since the thermal cycle test requires a temperature change from room temperature to 250–300°C, it can not estimate the coating's properties in a consistent temperature condition. So four-point-bend test is an alternative approach to test the properties of YSZ coatings.

The internal stresses within the thermal spray coating are caused by two main processes (Matejicek and Sampath, 2003; Tsui and Clyne, 1997). First, quenching stresses are developed during the deposition to fabricate the coating. As the molten particles strike onto the substrate or previous splats and immediately cooling down, the nonequilibrium thermal conditions produce large tensile stresses in the coating. Second, because of the difference of the coefficient of the thermal expansion between the coating and the substrate, after the cooling process, the mismatch force will be introduced and generate additional thermal stresses. Since the CTE of the ceramic coating is usually less than the metallic substrate, the stresses caused by the mismatch is generally compressive. For most YSZ-Al systems, due to the large CTE difference, the overall or net stresses at the room temperature within the coating are usually compressive although stress states vary locally due to high stresses generated during solidifications (Liu and Nakamura, 2006).

2.2 Four-point-bend test procedure

Figure 1 shows a schematic diagram of the four-point-bend test. Typical in-plane dimensions of the specimens are 230mm×25.4mm. The thickness of the coating varies from 250μm to 800μm. And the substrate thickness is usually 3mm. The outer supporting span ($2a+l$) is generally 120–160mm, and inner loading span l is set as 60mm. At the bottom of specimen, a laser with 1μm resolution is placed at the center of the beam to measure the displacement of the center point of the beam. The curvature of the beam can be calculated using beam theory (see Appendix). The coating layer should be placed facing down because tensile stresses are expected to be generated with the external moment added. During the loading test, the maximum displacement is chosen to control the maximum moment added to the beam. The maximum displacement should be not too

large to avoid the plastic deformation of the substrate (If the stresses in substrate reaches the yield stress, the loading curve before the plastic deformation can still be used to estimate properties, but the specimen will be failed and can not be used anymore).The feed rate of the loading indenter is chosen from 1–3mm/min, which depends on the maximum displacement required for the test. Since the limitation of the equipment, only 4 minutes experimental data can be recorded. So a larger maximum displacement requires a larger feed rate if more loading cycles are expected to be recorded. However a small feed rate can generate a smoother curvature change relation. At the beginning of the test, a 1.5–2N pre-load is needed to be added to confirm the loading indenters are thoroughly in contact with the beam. Since the unloading process will be more affected by the machine movement, the loading section is chosen to do the analysis.

Figure 2 shows a typical moment-curvature plot under loading process up to maximum moment 246N·m. The thickness of the coating is 463μm, while that of the substrate is 3.22mm. At the onset of the test, the coating is in compression owing to the mismatch of the coefficients of the thermal expansion (CTE). Since the loading test requires a 1.5–2N pre-loading, the initial curvature κ_R has to be measured before the loading process, which corresponds to the zero moment M_o point. As the loading moment increases, the stress in coating tends to change from compression to tension. Once the loading force reaches the maximum value, the beam will be unloaded (the unloading curve is not shown here).

An obvious nonlinear characteristic can be observed from the curvature-moment data. The curve becomes steeper as the external moment increases, which suggests a smaller stiffness of the coating under large tension. Although curvature-moment behavior is for the most part elastic, some specimens exhibit clearly different paths during loading and unloading phases. This cyclic hysteresis is likely to be caused by crack face sliding and associated friction and the properties of TS ceramics are more accurately described as ‘anelastic’ (Liu and Nakamura, 2006). The investigation of this phenomenon will be subject to a future publication. The non-linear behavior of the coating discussed in this paper is independent of these effects. In this study, the effects of various processing conditions on the nonlinear elastic behavior of coatings from their curvature-moment relations are presented, using a novel identification method.

3. Identification of nonlinear property

3.1 Constitutive model

In order to describe the coating's nonlinear behavior, a phenomenological constitutive model is introduced. First, based on the experimental observations and likely physical causes of nonlinearity (cracks and defects), the stress-strain relation should be set as asymmetrical under compression and tension. Second, under very large compression, the response should be nearly linear since many cracks and thin defects are closed. Thirdly, the transitional point from linear to nonlinear generally does not occur at zero stress ($\sigma = 0$). Since the experimental data suggest continues change of the coating stiffness, the following uniaxial stress-strain model is proposed:

$$\varepsilon = \begin{cases} \dfrac{\sigma}{E_C} - \dfrac{|\sigma_T|^n}{E_C \sigma_N^{n-1}} & \sigma < \sigma_T \\ \dfrac{\sigma}{E_C} + \dfrac{(\sigma - \sigma_T)^n - |\sigma_T|^n}{E_C \sigma_N^{n-1}} & \sigma \geq \sigma_T \end{cases} \tag{1}$$

Here, E_C is the elastic tangential modulus under small applied moment, n is the power-law exponent and σ_N is the reference stress. Also σ_T is the transitional stress where coating behavior change from linear to nonlinear although there is rather an approximated stress in real coatings. Generally this transition occurs at compression ($\sigma_T < 0$). If the transition is assumed to occur at $\sigma_T = 0$, the stress-strain relation simplifies to,

$$\varepsilon = \begin{cases} \dfrac{\sigma}{E_C} & \sigma < 0 \\ \dfrac{\sigma}{E_C} + \dfrac{\sigma^n}{E_C \sigma_N^{n-1}} & \sigma \geq 0 \end{cases} \tag{2}$$

The tension part of the model suggests a combination of the linear elastic model and a modified Ramberg–Osgood model.

Figure 3 shows a schematic stress-strain relation curve according to the (1). The stress-strain axes (σ^* - ε^*) centered at $\sigma = \sigma_T$ separates the linear and non-linear regimes. This model can describe many kinds of stress-strain behavior of TS coating with only

four parameters (E_C, n, σ_N and σ_T). With these parameters, the residual stress without external moment σ_R can also be determined.

The presented stress-strain model has been demonstrated suitable to describe the non-linear behavior of TS coating by many experimental data. It is a good model because it only requires four parameters while other models might need more.

3.2 Bimaterial beam solution under bending

The following section introduces a bi-material formula according to the beam solution to describe moment-curvature relation. According to this equation, a robust procedure which does not require large scale computations such as finite element analysis to extract unknown parameters of the coating can be developed. Although the procedure to identify unknown parameters is straightforward, the derivation of it is rather complicated due to the shift of the neutral axes of the coating as the stress changes (Liu and Nakamura, 2006). Furthermore, although there have been studies on large deformation effects on beams and plates (e.g., Finot and Suresh, 1996), a complete solution for the nonlinear elastic bi-material beams is fairly difficult to find out.

Suppose a bi-material specimen consists nonlinear elastic coating and linear elastic substrate as shown in figure 4. The axial strain in the coating corresponding to the curvature is:

$$\varepsilon_c(y) = -\kappa(y - y_0) + \frac{F_{mis}}{bE_c^* t} = -(\kappa_M + \kappa_0) + \frac{F_{mis}}{bE_c^* t} \tag{3}$$

Here, κ is the curvature of the substrate measured by the laser, κ_M is the curvature generated by the external moment loaded by the machine, κ_0 is the curvature developed by the mismatch force, y_0 is the location of the neutral axis, b is the width of the specimen, t is the thickness of the coating, F_{mis} is the mismatch force needed to equilibrate thermal expansions of coating and substrate, E_c^* is the secant modulus, defined as $E_c^* = \sigma_c / \varepsilon_c$.

The neutral axis y_0 changes as the secant modulus changes:

$$y_0 = \frac{E_S h^2 / 2 + \int_h^{h+t} E_c^*(y) y dy}{E_S h + \int_h^{h+t} E_c^*(y) dy} \tag{4}$$

Here, E_S and h are the Young's modulus and thickness of substrate, respectively. The moment-curvature relation for the bi-material beam is:

$$\Delta\kappa = \frac{\Delta M}{I_E} \tag{5}$$

Here, ΔM can be the mismatch moment caused by the mismatch force or the external moment added by the loading machine. I_E is the stiffness of the bi-material beam which is not a constant. It can be computed as:

$$\frac{I_E}{b} = E_S h\left(\frac{h^2}{3} - hy_o + y_0^2\right) + \int_h^{h+t} E_C^*\left(y - y_0\right)^2 dy \tag{6}$$

If assuming that the integral of the secant modulus E_C^* can be replaced by the average modulus E_{ave}^* through the coating thickness, the location of neutral axis can be expressed as:

$$y_0 = \frac{E_S h^2 + E_{ave}^* t^2 + 2E_{ave}^* ht}{2\left(E_S h + E_{ave}^* t\right)} \tag{7}$$

Then the moment-curvature equation can be reduced to the following formation:

$$\Delta\kappa = \frac{12\left(E_S h + E_{ave}^* t\right)}{{E_S}^2 h^4 + (E_{ave}^*)^2 t^4 + 2E_S E_{ave}^* ht\left(2h^2 + 3ht + 2t^2\right)}\Delta M \tag{8}$$

A similar assumption can be taken for the computation of y_0 in (4). To further reduce the computational requirement, instead of computing the correct average value, E_{ave}^* can be estimated at the midpoint of coating ($y = h + t/2$) as:

$$E_{ave}^* = \frac{\sigma(\varepsilon_c^{mid})}{\varepsilon_c^{mid}} \text{ , where } \varepsilon_c^{mid} = -\kappa(h + \frac{t}{2} - y_0) + \frac{F_{mis}}{bE_c^* t} \tag{9}$$

Clearly that the computation of E_{ave}^* is still need multiple iterations.

The equations above use mismatch force as a parameter to calculate axial strain. However in the actual computational process, only the relation between strain and curvature is needed. So a relation between mismatch force and initial curvature needed to be established to cancel out this unknown mismatch force.

The mismatch force F_{mis} can be computed using the following procedure (details will be explained in appendix). Suppose at the fabrication process, the substrate is heated

up and extends to the length L^*, and at this time, the coating is sprayed onto the substrate. After the fabrication, the beam cools down to the room temperature. Suppose the substrate and the coating will shrink to the length $L - L_0$ and L, respectively (generally, the coefficient of the thermal expansion of the substrate is larger than the ceramic coating) (Matejicek and Sampath, 2003; Tsui and Clyne 1997). Then the mismatch force and axial strain can be expressed as:

$$F_{mis} = \frac{L_0 E_C E_S A_C A_S}{L E_S A_S + (L - L_0) E_C A_C} \tag{10}$$

$$\varepsilon_C^{mis} = -\frac{F_{mis}}{E_C A_C} = \frac{L_0 E_S A_S}{L E_S A_S + (L - L_0) E_C A_C} \tag{11}$$

Since the mismatch force will cause an internal moment, the beam will have an initial curvature, which is related to the thickness of the beam. Suppose the mismatch forces are loaded at the centers of the coating and substrate layers, the internal moment per-thickness can be expressed as:

$$M_i = \frac{F_{mis}}{b}\left(\frac{t+h}{2}\right) \tag{12}$$

where b is thickness of the beam. With the moment-curvature relation $\kappa = M / I_E$, the initial curvature introduced by mismatch force is:

$$\kappa_0 = \frac{L_0 E_C E_S h t}{L E_S h + (L - L_0) E_C t} \cdot \frac{t+h}{2} \cdot \frac{1}{I_E} \tag{13}$$

Because the initial axial stress in coating is the combination of mismatch in length and the initial curvature and then it increases with the external moment, so the final expression of the axial strain in coating is:

$$\varepsilon_C = \frac{2 I_E \kappa_0}{E_C t (h+t)} - \kappa (y - y_0) \tag{14}$$

Here, κ is total curvature which can be measured by the laser, κ_0 is the initial curvature measured prior to the four-point-bend test. Equation (14) will be used to calculate the axial stress in coating and the residual stress.

Figure 5 illustrates the process to calculate the curvature change for a given moment. The calculations of stresses and secant modulus are described in the appendix.

3.3 Estimation procedure for unknown properties

There are four unknown parameters (E_C, n, σ_N and σ_T) in the proposed model needed to be determined. A multi-step procedure is proposed here to estimate these parameters. First, the tangential modulus in the linear section is computed. In order to calculate this modulus, the transitional point is needed to pick out. Using the slope the linear portion of the curve, the modulus can be computed by solving the following equation:

$$\Delta\kappa = \frac{12\left(E_S h + E_C t\right)}{{E_S}^2 h^4 + {E_C}^2 t^4 + 2E_S E_C ht\left(2h^2 + 3ht + 2t^2\right)}\Delta M \tag{15}$$

Next, the nonlinear parameters n and σ_N are determined by inverse analysis. Here, to make the process simple, the moment and curvature coordinates can be shifted to $M^* = M - M_T$ and $\kappa^* = \kappa - \kappa_T$, respectively. With this shifting, the nonlinear parameters n and σ_N can be computed using equation (2) instead of the complicated form (1). Also, due to the shifting, the strain in the coating needs to be updated using the equation $\varepsilon_c^{mid} = -\kappa(h + t/2 - y_0)$ instead of the expression in (9). The stress and strain are re-adjusted once the parameters determined. Kalman filter algorithm is used to estimate the parameter n and σ_N, which will be explained in the next paragraph. Once the other three parameters are determined, the transitional stress σ_T can be solved and also the residual stress when the moment is zero. The detail will be explained in appendix.

3.4 Kalman filter

Obviously, the reference stress σ_N and power-law exponent n cannot be calculated directly from the moment-curvature input because there is no direct relation between them. The approach to estimate these unknown parameters is utilizing inverse analysis. The inverse analysis is the method to estimate unknown parameters from indirect measurements. The inverse analysis used in this study is Kalman filer (Kalman 1960).. The Kalman filter algorithm has an advantage over other adaptive algorithms through its fast convergence to optimal solutions in nonlinear problems (Liu and Nakamura, 2006). Essentially it updates the previous estimates based on the indirect measurements of unknown state variables and covariance information and attempts to find the best

estimate. In the formulation, two unknown parameters are represented in a state vector form as $x_t = \left[(\sigma_N)_t, n_t\right]^T$. Here, *t* represents the actual time or the increment number. The procedure is carried out with the following updating equation:

$$x_t = x_{t-1} + K_t\left[\kappa_t^{meas} - \kappa_t(x_{t-1})\right] \tag{16}$$

Here, $\boldsymbol{K}_t$ is the 'Kalman gain matrix' and κ_t^{meas} is the measured curvature at *t*. Also $\kappa_t(\boldsymbol{x}_{t-1})$ is a curvature computed with estimated state parameters at the previous increment. In the above equation, the Kalman gain matrix multiplies the difference between the measured and computed curvature to make corrections to the unknown state parameters. The Kalman gain matrix is computed as:

$$K_t = P_t(\kappa_t')^T R_t^{-1} \quad \text{where} \quad P_t = P_{t-1} - P_{t-1}(\kappa_t')^T(\kappa_t' P_{t-1}\kappa_t'^T + R_t)^{-1}\kappa_t' P_{t-1} \tag{17}$$

With two state parameters and one measured parameter, the size of the Kalman gain matrix is 2×1. Also κ_t' is a vector that contains the gradients of κ_t with respect to each parameter:

$$\kappa_t' = \frac{\partial \kappa_t}{\partial x_t} = \begin{pmatrix} \dfrac{\partial \kappa_t}{\partial \sigma_N} \\ \dfrac{\partial \kappa_t}{\partial n} \end{pmatrix} \tag{18}$$

In addition, P_t is the measurement covariance matrix related to the range of unknown state parameters, and R_t is the error covariance matrix related to the size of measurement error. Once the initial values are imposed, P_t is updated at every step, while R_t is prescribed at each step. In many cases, fixed values can be assigned to R_t as long as measurement error bounds do not vary substantially. As the convergence rate is sensitive to the values of P_t and R_t, proper assignments for these two matrices are essential. The initial measurement covariance matrix P_0 is set according to the estimated ranges of state parameters (i.e., domain of unknowns), while the constant error covariance matrix R_t is chosen based on the estimated measurement error for the curvature measurements (~1% of total curvature change).

In many inverse analyses, forward solutions are constructed through finite element computations for some combinations of state parameters. However in this

problem, the curvature–moment has been established, and the required parameters κ_t in (17) and κ_t' in (18) can be obtained without complex computational analyses. Figure 6 shows the procedure to carry out Kalman filter to estimate unknown parameters, which is functioned by a computational code.

4. Verification study

Before using this proposed procedure to estimate real TS coatings, many finite element simulations were carried out to verify the robust of the procedure. Because the parameters of the FEM model are known, the comparison of the results from the inverse analysis with the input parameters can exam the accuracy and robustness of the procedure.

4.1 Finite element procedure

4.1.1 Model and material properties

In the four-point-bend test, the major purpose is to generate a uniform stress-strain state within the inner loading span, which is convenient to evaluate the stress-strain and moment-curvature relation. So in the finite element analysis, the dimension of the FEM model is unnecessary to be exactly the same as the sample. However the thicknesses of the layer and the substrate should be the same as the specimen because those two parameters impact the inverse analysis result. Many FEM models were generated to exam the accuracy of the procedure. Here, an example which the length of the beam is 50mm, the thickness of the coating is t = 488μm and that of the substrate is h = 3.256, is presented here. There are total of 26700 elements in the mesh. While in the coating layer, very small elements were used because of its nonlinear behavior. If the elements are too large, there will be inconsistent results from the bending test. Figure 7 shows the finite element model used to do the simulation.

In the test, the substrate plate is Al6061 whose Young's modulus is E_S = 69GPa. Nonlinear elastic properties of the coating are defined by the parameters E_C, n, σ_N and σ_T. The coefficient of thermal expansion (CTE) is set for substrate. Although there is no temperature change during the four-point-bend test, the CTE was used to impose the residual/initial curvature of the plate. Since it is only needed to set the residual curvature and stress at the room temperature, the value and corresponding cool-down temperature are set arbitrary to match closely with the experimental measurements. In the first step of the FE analysis, the temperature is lower to cause the residual stresses prior to any mechanical load application.

4.1.2 Boundary and loading conditions

Because of the symmetry, only half side of the beam was modeled and proper boundary conditions were prescribed. In the finite element analysis, a different loading condition is used. In the four-point-bend test, the moment is added using the inner and outer support. According to this loading condition, only the small portion of the beam within the inner loading span was added a uniform moment to develop a consistent stress-strain status. However, since the mission of the analysis is to extract a relation between moment and curvature, so any kind of loading is acceptable only if it can generate a uniform moment-curvature relation within the coating layer. In this analysis, a pair of point force which has same magnitude but reverse directions added at the upper right corner and lower right corner of the model was used to simulate the moment added to the beam. With this loading condition, almost the whole beam was loaded with a uniform moment, so the moment-curvature relation is more convenient to find out. This loading condition is better than the four-point-bend loading because it can minimize the boundary effect and generate a larger part of the uniform moment-curvature condition and the result of it is the same as four-point-bend loading condition. The schematic diagram of the loading condition is shown is figure 8.

4.2 Simulated moment-curvature records and estimated nonlinear properties

The moment added to the coating is $M = P(h+t)$, where P is the force added and t and h are the thickness of the coating and substrate. The curvature of the beam is computed using the deflection of a chosen point A in the bottom surface of the substrate. The curvature of the substrate can be computed as: $\kappa = 2v/l^2$, where v is the vertical deflection at the point A and l is the distance between the center and A.

Before adding the moment, the temperature was lower down to a negative value to generate an initial curvature. With this condition, the stress in coating will be firstly in compression, which is the known as the residual stress. This is the same situation as in the real specimen after the fabrication process. The residual stress was recorded to compare with the estimated value since it is a very important parameter to study the property of beam. Then the moment was added to a limited value. The stress in coating

will change from compression to tension. Also the curvature of the beam will become larger. Record the curvature change corresponding to the specific moment, and this relation is the input information to do the inverse analysis.

Figure 9 shows three moment-curvature relations from FEM results corresponding to three different nonlinear properties. The Young's modulus of the substrate was set the same as Al6061 (69GPa). The moment of all these analysis were added to around 400N·m, corresponding to the actual experimental value. A too large moment will make the substrate deform plastically, which could cause the beam fail. In real test, this situation should be avoided.

The stress-strain relations were also recorded from finite element analysis. Since the stress and strain are distributed differently along the vertical direction in the coating layer, the mid-plane of the coating was chosen to represent the average stress-strain change in the coating, which corresponds to the computation of the average Young's modulus of coating E^*_{ave} in (9). The comparison of these results with the estimated stress-strain relations can show the accuracy of the evaluation.

With the moment-curvature relation input, the inverse analysis was carried out to estimate the nonlinear properties of the coating. Many sets of input parameters were carried out to exam the robustness of the procedure. To avoid making the paper to long, only three cases are presented as examples. Before carrying out the Kalman filer process, a transitional moment which corresponding to the transitional point from linear to nonlinear portion has to be selected as another input value to do the analysis (as shown in figure 10). The selection of this point extremely affects the inverse analysis result. And by observing the moment-curvature relation presented before, the transitional point is not that obvious to select. However, our study demonstrated that if the transitional moment M_T can be selected in a small range, the estimated process was not that strongly affected by the accuracy of the selection. This will be shown in later paragraph. Once the transitional moment was selected (in case 1, $M_T = 30\text{N}\cdot\text{m}$), the linear slope of between transitional moment and zero moment was used to compute the initial Young's modulus by solving (8) (Here $E^*_{ave} \approx E_C$). In case 1, the Young's modulus was computed as 26.3GPa, which is 5.9% off from the imposed modulus (28GPa).

The next step is to calculate parameters σ_N and n using Kalman filter procedure introduced in part 4. First, reset the moment-curvature coordinates to $M^* - \kappa^*$ as shown in figure 10. 30 moments and curvatures were selected equivalently between zero moment and maximum moment as the Kalman filter inputs. The initial estimate of σ_N was selected within the range of $10\text{MPa} < \sigma_N < 40\text{MPa}$ while the range of n was selected as $1 < n < 4$. Note these selections are only initial trials. If the final estimates were out of the domain selected above, the range should be adjusted to a proper domain. Next, σ_N and n were incremented to forty separate values to generate 41×41 = 1681 sets of initial estimates. Each set of initial estimates is processed through Kalman filter and the final estimates were obtained after 30 steps. Generally, the final estimates of different initial points are not the same. However, if the procedure is robust enough, the final estimates should generate a small domain of convergence. The intensity of convergence created by the 1681 initial values is plotted in figure 11. Here, high intensity region implies greater convergence of initial estimates. The highest intensity of convergence location (σ_N = 19.3MPa, n = 3.56) can be selected as the best estimates as shown in the figure (where the input values are σ_N = 20MPa, n = 3.5).

The remaining parameters can be calculated once the above values are obtained. The transitional stress computed is σ_T = –10.4MPa (3.9% lower then input value –10MPa). And the residual stress is calculated as σ_R = –20.1MPa (0.3% off from –20MPa). With these parameters calculated, the stress-strain relation can be re-constructed according to the (1). Figure 12 shows the estimated stress-strain relation compared with the input stress-strain relation. It is clearly to see that for the linear portion, the agreement of the two stress-strain curves is very good. However for the nonlinear portion, the difference between estimated stress-strain relation and exact relation can not be neglected, which estimated curve shows more compliant as the stress increases. Even though the estimated stress-strain relation have a serious difference from the input relation, a good agreement between the re-constructed moment-curvature relation using the best estimates as input parameters (Liu and Nakamura, 2006) and the input moment-curvature relation proves that the estimation is accurate (as shown in figure 13.)

Since all the four parameters impact the stress-strain relation and the estimate of all them are not that accurate, many more simulations were carried out to exam the influence of each parameters. Here two more cases with different input parameters are presented in table 1. And the estimated stress-strain relation and input relation are also plotted in figure 14.

From the results we can find that the estimation of transitional stress σ_T and residual stress σ_R is very accurate. Although the error of the estimate of initial modulus E_C is not that small, it can still remain within the range of ±5%. And because the estimate of initial modulus used a linear algorithm, the estimation of it is stable.

The results from table 1 also show that the estimation of reference stress σ_N and power-law exponent *n* has a serious oscillation. Especially for power-law exponent *n*, the estimated error can go up over 10%. This instability of estimation of these two parameters extremely impacts the simulation of stress-strain relation. To study the reason of the instability of the estimation, more simulations were carried out and will be discussed next.

4.3 Sensitivity of estimated results

Since there are potential errors in determining the unknown parameters, the sensitivities of estimated results are closely investigated.

4.3.1 Variation in nonlinear parameters

The method to study the influence of the reference stress σ_N and power-law exponent *n* is to generate different moment-curvature relations according to different σ_N or *n* while all the other parameters are given the same value.

Figure 15a shows the plots of moment-curvature relation which the reference stress varies from 10MPa to 80MPa while other parameters have the same value (E_C = 28GPa, n = 2.5, σ_T = −10MPa). It is observed from the figure that the curvature of the beam has obvious difference at the same moment added when reference stress are different. Although the different moment-curvature curves seem overlap each other when the moment is less than 100N·m, they start to scatter and show a significant difference

when the moment goes up to around 200N·m. So the differences of performance of YSZ coating for different reference stress result in a better estimation of σ_N (error less than 5%).

Figure 15b is the moment-curvature plots which power-law exponent varies from 1.5 to 3.5 where other parameters are E_C = 28GPa, σ_T = −10MPa, σ_N = 20MPa. From the result we can conclude that even though the power-law exponent has different values, the curvatures of different specimen loaded with the same moment do not have that much variability. In another word, even though the power-law exponent n has different values, the moment-curvature relations are almost the same as they go up approximately along the same route. Although the curvatures of the beam show larger differences when the moment goes up to 800−1000N·m, in actual four-point-bend test, this large moment can not be reached because of the plastic deformation of the Aluminum substrate. Due to the closeness of the performance of the specimen, when the moment-curvature relation is used as input of the Kalman filter procedure, the algorithm can not give out an accurate estimate of n.

However, although the errors in estimation of reference stress and power-law exponent extremely impact the accuracy of the stress-strain relation, the estimated result is still very useful by carefully observing the re-construction curve carefully. The estimated stress-strain relations in figure 12 and 14 indicate that the estimated curves always have smaller slope than the actual inputs as the stress increases. This phenomenon indicates that the estimated stress-strain relation shows a more compliant behavior than the real property. So when the stress of the coating reaches some value, the actual strain in coating is smaller than the estimated value. In this condition, if the failure criteria of the TS coating is according to the maximum stress it suffered, the coating will be in a safer status.

4.3.2 Variations in transitional point

As discussed above, a transitional point has to be selected prior to the analysis procedure, which is a very important input for the estimation. However, although the moment-curvature relation of the TS coating is clearly a combination of a linear portion and a nonlinear portion, the transitional point is not that obvious. So the procedure is

robust only if the estimated parameters do not vary too much when selecting the transitional point in an acceptable range.

To evaluate the influence of the transitional point, a moment-curvature relation with parameters E_C = 28GPa, σ_T = −10MPa, σ_N = 30MPa, n = 2.5 was used to carry out the inverse analysis. The exact transitional moment is M_T = 50N·m. So a range from 40−60N·m was selected to exam the stableness of proposed procedure.

Table 2 lists the estimated parameters and errors with different transitional moments selected. It shows that the estimated parameters are acceptable if the transitional moment is selected within the range 50±10N·m. From figure 16 we can notice that it is a pretty wide range that can guarantee a suitable value can be selected as transitional moment. So although the transitional point is not that obvious to select, the procedure can ensure a robust result if the transitional point is selected in a small range.

5. Comparison study with thermal cycle test

Thermal cycle test is an effective method to estimate nonlinear parameters of TS coatings. To study the effectiveness and accuracy of four-point-bend test, the comparison of the computation procedure of two tests is necessary. The comparison study includes the calculation of modulus, sensitivity of random errors and stress variation within coating.

5.1 Effects of measurement error on initial modulus

In four-point-bend test procedure, initial modulus E_C is computed by solving the quadratic equation (15), where $[\Delta\kappa/\Delta M]_{\text{initial}}$ is the initial slope of moment-curvature curve before transitional point. There are four parameters in (15): coating thickness t, substrate thickness h, Young's modulus of the substrate E_S, and slope $[\Delta\kappa/\Delta M]_{\text{initial}}$. The impact of measured errors of these parameters is required to be observed carefully.

To examine the influence of these four parameters, a simulated moment-curvature relation was generated with the parameter: h = 3.256mm, t = 0.488mm, E_S = 69GPa, $[\Delta\kappa/\Delta M]_{\text{initial}}$ = 0.00405$(\text{N}\cdot\text{m}^2)^{-1}$, and the initial modulus E_C calculated is 30GPa. Then ±1% errors were added to each parameter to re-calculate the initial modulus. The results listed in table 3.1 indicate that only 1% error in substrate modulus or liner slope will generate a 4–5% error in the value of E_C computed. And for substrate thickness, a 1% error may generate 15% error to E_C.

Comparing with this result, initial modulus error sensitivity of thermal cycle test was also studied. In thermal cycle test, the quadratic equation used to solve initial modulus is:

$$\frac{\Delta\kappa}{\Delta T} = \frac{6E_s E_c ht(h+t)\Delta\alpha}{E_s{}^2h^4 + E_c^2t^4 + 2E_sE_cht\left(2h^2+3ht+2t^2\right)} \tag{19}$$

With the same parameter h = 3.256mm, t = 0.488mm, E_S = 69GPa and $[\Delta\kappa/\Delta T]_{\text{initial}}$ = 0.001273$(\text{m}\cdot°\text{C})^{-1}$ input, E_C is calculated the same value 30GPa. By adding ±1% errors to these parameters, the initial modulus calculated is listed in table 3.2.

From the results we can see that 1% error in these parameters only generate 1–2% error in calculation of E_C.

This analysis indicates that for four-point-bend test, the calculation of initial modulus is very sensitive to the substrate thickness h, Young's modulus of the substrate E_S, and the slope $[\Delta\kappa/\Delta M]_{\text{initial}}$. So to carry out the experiment, the precision of these parameters is highly required. And a small error of these parameters might result in an incorrect estimation.

Another analysis was carried out to see the difference of linear slopes for different initial modulus. In the analysis, initial modulus was set to vary from 5–30GPa while all the other parameters have fixed values. The moment-curvature curves were plotted in figure 17. The initial slopes between initial curvature and transitional curvature for different initial modulus have very slight differences. The similarity of the behavior for different initial modulus makes the calculation of initial modulus is extremely sensitive to the measurement errors. An improper initial modulus value might be computed if there are small measurement errors in initial slope.

5.2 Effects of random measurement errors

The experimental errors in the four-point-bend test can be generated by the force recorder because of the instability of the displacement control or by the laser recorder. Since the moment-curvature relations of different parameters do not have too much difference themselves, the procedure's sensitivity of the measured errors is more important to exam. By adding a random error to the simulated curvature data, the estimated parameters can reflect the sensitivity of the procedure. To compare the error sensitivity with the thermal cycling test, the same error bound was added to the simulated temperature–curvature record. Randomly artificial errors within ±5μm were added to the deflection measurements. According to the equations converting deflection to curvature ($\kappa = 2v/l^2$), the error of deflection translates to error of curvature of $\pm 0.002 \text{m}^{-1}$ in thermal test and $\pm 0.0106\ \text{m}^{-1}$ in four-point-bend test. Notice here that the error bound of four-point-bend test is 5.3 times of that of thermal test. This is because for the same deflection, the curvature is inversely proportional to the square of the span where the span of thermal

test is l = 69mm, while the span of four-point-test is l = 30mm. In this situation, the error bound of four-point-bend test is $(6.9/3)^2 \approx 5.3$ times of that of thermal cycle test.

The estimated errors can show the stability of the inverse analysis procedure. A serious oscillation of the estimated results indicates the procedure is very sensitive to the measurement error, which is not robust enough. 5 sets of different random errors were added to the simulated recorded for both thermal cycle test and four-point-bend test. And three materials with different parameters were selected in this verification study. The parameters of them are: E_C = 31GPa, σ_N = 51MPa, n = 3.23, σ_T = –31MPa; E_C = 30GPa, σ_N = 15MPa, n = 2.46, σ_T = –11MPa; E_C = 23GPa, σ_N = 29MPa, n = 2.88, σ_T = –17MPa.

Another point should be mentioned here is that since the calculation of initial modulus does not use Kalman filter, the linear portion of the moment-curvature data was not added with errors. Since the value of the initial modulus can significantly affect the estimation of power-law exponent and reference stress, no error added for linear portion can result in a relatively accurate initial modulus, thus minimize the effect of the initial modulus. In another word, the result of the estimation correctly shows the error sensitivity of the Kalman filter procedure. And this is the same for the temperature-curvature data – no artificial error was added to the linear portion of the temperature-curvature record. An example of temperature-curvature plot and moment-curvature plot with artificial error added are shown in figure 18.

Tables 4a-c show the estimated results for three different materials with artificial errors added. The initial modulus was estimated exactly the same as input value, so this parameter does not affect the estimation of the other three parameters. Figure 19 plots the estimated errors corresponding to no measurement error case and five artificial error added cases for material I. It can be observed from the figure that the thermal cycle test is less sensitive to errors because the estimated errors of the power-law exponent and reference stress is smaller than that of four-point-bend test. Actually the four-point-bend test shows very unstable estimated results with the artificial errors included. The largest error can go up to around 18%, while the average error can also larger than 10%. However although the thermal cycle test also shows a big influence by the errors, the largest average estimated error is just around 5%, and the other two materials only show less than 3% estimated errors. The estimation of the transitional stress is the very late step.

And the results show that both thermal cycle test and four-point-bend test can have a very good estimation of transitional stress. Even though the estimated values from four-point-bend test are stable, the errors for both tests are generally smaller than 2%. So we can conclude that the four-point-bend test is more sensitive to the measurement errors than thermal cycling test.

This can be explained by the previous analysis in Section 4.5. When suffering the same moment, the curvatures of the specimens with different parameters do not differ that much. Especially for power-law exponent, the curves of moment-curvature records almost overlap each other from the results shown in figure 15(b). So a small different of the curvature may result in the different parameters from the inverse analysis. This feature of the power-law exponent makes the estimation extremely difficult if there is measured error. And this is demonstrated by the results that the difference between estimated values of power-law exponent and input value is bigger than the difference for reference stress. So for the four-point-bend test, decreasing measured errors is necessary to increase the estimated accuracy.

The determination of the transitional stress is carried out at the latest step. And the results from the table show that both thermal cycle test and four-point-bend test can have a good estimation of transitional stress. For both tests, the estimated errors are smaller than 5%. However, the estimation from the four-point-bend test is even more precise. For both estimations, the transitional point chosen is the exact value, so the influence of the selection of the transitional point is eliminated. The reason why the four-point-bend test can give a better estimation is it used an improved algorithm to calculate transitional stress (see appendix). For both tests, the calculation of transitional stress depends on the estimated value of reference stress σ_N and power-law exponent n. However in the thermal cycle test, the calculation of transitional stress mainly depends on the nonlinear portion of the curve, in another word, the two nonlinear parameters σ_N and n. While in the bending test, the calculation mainly depends on the linear slope or the initial modulus, and the nonlinear parameters have a relatively small influence on the calculation of the transitional stress. So in the bending test, although the estimation of the σ_N and n changes a lot, the estimated value of transitional stress σ_T does not change too much. This improved algorithm can give a relatively consistent estimation of transitional stress,

especially in the process of real experimental data, since the selection of the transitional point can not be selected as the exact point, this is improvement is more valuable.

5.3 Stress variation within coating thickness

In proposed method, the modulus of coating was approximated using the average secant modulus in the mid-plane of coating layer: $E_c^*(y) \cong E_{ave}^* \cong \sigma_{mid}^* / \varepsilon_{mid}^*$. This approximation is proved very effective in thermal cycle test. However in four-point-bend test, the variation of stress through coating thickness has to be considered.

Since the axial stresses in the coating layer will change gradually through the thickness, the axial stresses at the bottom, middle and top plane in coating layer for both four-point-bend test and thermal cycle test are plotted in figure 20 to represent the stress variation in coating. As indicated in figure 20(a), in four-point-bend test, the difference of the axial stresses at the three planes is significant and becomes larger as the moment increases. However in thermal cycle test, the axial stresses at the three planes almost remain the same as the temperature increases from room temperature (25°C) to highest temperature (around 250°C). This feature can be observed more clearly in figure 21. Figure 21 shows the axial stress differences between mid-plane and different positions of coating layer through coating thickness. It clearly shows that in four-point-bend test, the axial stresses through coating differ significantly, and when the moment reaches the maximum value, the largest difference can go up to 2MPa. However for thermal cycle test, the largest difference is only 0.5MPa. Because of the large variation in axial stress through coating thickness, when calculating the secant modulus of the coating, the approximation $E_c^*(y) \cong E_{ave}^* \cong \sigma_{mid}^* / \varepsilon_{mid}^*$ may generate larger error in estimates.

6. Nonlinear properties of thermal spray YSZ coatings

After the verification study, the procedure was carried out to analyze the experimental moment-curvature data to estimate the nonlinear properties of the thermal spray coatings. Here, the analysis result of specimen #1076-1 (coating thickness: 463μm; substrate thickness: 3.22mm) is used demonstrate the inverse analysis procedure.

6.1 Estimated properties under four-point-bend tests

The measured moment-curvature plot of specimen #1076-1 is shown in figure 22. The maximum moment added was 246N·m. The transitional moment selected is 40N·m. Using the linear slope of the moment-curvature curve, the initial modulus was computed as E_C = 19.1GPa. By re-adjusting the coordinates to $M^*-\kappa^*$, the σ_N and n were estimated by processing Kalman filter introduced in Part 4. The intensity of convergence plot is shown is figure 23. The best estimates are σ_N = 50.9MPa and n = 3.9, respectively. The transitional stress and residual stress are also obtained as σ_T = –6.4MPa and σ_R = –13.1MPa, respectively.

Use theses parameters, the stress-strain relation is shown is figure 24. The residual stress (moment is zero), transitional stress and maximum stress (maximum moment) are marked out with small cycles. Essentially, the slopes outside these points represent extrapolated results since only the records between minimum and maximum moments were actually used to identify the unknown parameters. These bounds are important since the actual coatings may act differently outside the range, especially under large tensile stress (e.g., cracking).

In most inverse analyses, there is no independent way to prove that best estimates are indeed correct or near-correct solutions. However, there are two ways to judge their accuracy. One is using the best estimates as input parameters to re-create moment-curvature relation (as mentioned before). The agreement with the measured curvature is excellent as the re-constructed curve fits within the bound of measurements. Another way is from the sizes of converged regions shown in the intensity of convergence plot (Liu and Nakamura, 2006). A small region implies the robustness of inverse method as many

initial estimates converged near the same location (i.e., similar estimates). The converged region shown in figure 23 is well contained and supports the accuracy of the estimates.
Many experiments (including HOSP and FC specimens) were carried out to estimate the properties of YSZ coating under four-point-bend test, and the measured moment-curvature relations are plotted in figure 25a. Table 5 lists the estimated parameters for HOSP and FC specimens.

It can be clearly observed from the table that FC specimens generally have larger initial elastic modulus (35−50GPa) than HOSP specimens (10−30GPa) under pure bending test. And also, nonlinear degrees of FC specimens are relatively smaller (~<1.1) compare to the HOSP specimen (1.1−1.2). This feature indicates that FC specimen is expected to exhibit much stiffer behavior than HOSP specimen under pure bending condition. And this characteristic is also reflected from the estimated stress-strain relations for HOSP and FC specimens in figure 25b. Generally, the slope of FC stress-strain curves is steeper than that of HOSP stress-strain curves, which indicates that in compression, FC specimens have a greater initial modulus and exhibit a stiffer behavior in tension than HOSP specimens.

Another observation from the table is that normally FC specimens have a very high transitional stress (~> −1MPa) than HOSP specimens (~ −6 - −1MPa) which might be caused by the different microstructure of the two spray powders.

In order to clearly distinguish the similarities or differences among coatings, 'nonlinear degree' (ND) is defined t as (Liu, et al 2008):

$$\mathrm{ND} = E_C / E^*_{0.001} \tag{20}$$

Here E_C is the initial elastic modulus defined in (1) and $E^*_{0.001}$ is the secant modulus between the transitional point (σ_T, ε_T) and the stress and strain at $\varepsilon = 0.001$. With this definition, a large ND value signifies greater nonlinearity while ND = 1 if a coating is linear elastic. The parameter essentially represents the departure of stress-strain relation from its initial linear slope. The computed values are listed in table 5 and the modulus-nonlinear degree diagram for these specimens is shown in figure 26.

6.2 Repeatability check

To examine the consistency of measured results, separate tests were carried out on same specimens. To ensure the repeatability of procedure, the specimens were taken out of the apparatus after each measurements and then placed back to test again. Very similar moment-curvature relations are obtained from the separate tests as shown in figure 27 for HOSP #1076-3 specimens. These records were processed and estimated material parameters were listed in Table 6. The estimated stress-strain relations in figure 28a indicate that even the input moment-curvature relations are very similar, the results have small difference. One reason for this feature is the four-point-bend test is very sensitive, so the estimated errors may generate the difference in the estimation. Another reason is that by carefully observing the stress-strain relations, it can be found that the coating becomes softer as the test number increases. This indicates that the high stresses generated within the coating layer already changed the microstructures of coating. For HOSP specimen, once the cracks open up or the slides happen under high stresses, it may not be able to go back to the original status again. And coatings will show softer behavior if it is loaded second time.

The repeatability was also tested with FC #1078-4 specimens and its estimated properties from three separate tests are listed in Table 6 and the corresponding stress-strain relation shown in Figure 28b. Still the behaviors of the coatings show difference between three tests. But not like HOSP specimens, FC specimens do not show obvious softer behavior as the test number increases. So for FC specimens, although four-point-bend test will change the coating behavior a little bit, the estimated results are unstable. The computed nonlinear degrees for the two specimens are shown in figure 29. An obvious observation from the figure is that for the FC and HOSP specimens, elastic modulus shows a good repeatability. But nonlinear degree varies a lot for different tests due to the change of the microstructure of the coatings.

6.3 Comparison with thermal results

Figure 30 shows a comparison of the estimated stress-strain relation between the thermal cycle test and four-point-bend test for specimen #1076-1. The estimated parameters of specimen #1076-1 are E_C = 17.8GPa, σ_N = 10.5MPa, n = 2.61, σ_T =

–6.2MPa after carrying out the inverse analysis for thermal cycle test (Liu and Nakamura, 2006). The significant difference between the two curves indicates that the YSZ coating will perform differently under pure mechanical bending test and thermal test. In compression, the secant elastic modulus of YSZ coating is almost the same under pure bending or thermal test. This indicates that in compression when the cracks and other defects within the coating closed, the properties of the YSZ coating barely affected loading condition. And the transitional stresses for both tests are almost the same. However, YSZ coating shows a very different behavior when suffering tensile stress. In tension, YSZ coating always shows much larger secant modulus when suffering the pure bending load then increasing the temperature. This is a very important phenomenon that YSZ coating will behave much stiffer when suffering the pure mechanical loading at the room temperature than in the condition of increasing the temperature. The properties of other specimens determined from thermal cycle test are listed in table 7. An observation from the results in table 5 and 7 is that the residual stresses of all the specimens from both thermal cycle test and four-point-bend test are almost the same. This is because residual stress is only related to the manufacturing process of the coating, and it is corresponding to the residual curvature. So for the same specimen, since the residual curvature is the same, the residual stresses estimated from both tests are almost the same.

The different behaviors from bending test and thermal cycle test are mainly from two reasons: 1) in thermal cycle test, almost the whole specimen is in consistent stress-strain status. But in four-point-bend test, since only a small region within the inner loading span is loaded with constant moment, the stress-strain relation within that range can be affected by the boundary condition significantly; 2) Two test has different method to add moment to the coatings: in thermal cycle test, the moment is generated from the mismatch force between coating layer and substrate. It can be seen as an inner moment. And in four-point-bend test, the moment is generated by the external loading devices. When the loading support in contact with coating, it may change the coating's properties already.

The characteristics of each coating's behavior under mechanical loading and thermal loading can be summarized graphically, as shown in figure 31. In this figure, 'nonlinear degree' (ND) is plotted as a function of the initial modulus E_C for each

specimen to compare the different behavior of the coatings. Clearly from the figure that under four-point-bend test, the nonlinear degree is much smaller (1.1–1.2) than under thermal cycle test (1.7–2.5) for both HOSP and FC specimens, which indicates that the YSZ coating behave much stiffer under pure mechanical loading condition than under thermal loading condition. For HOSP specimen, the initial elastic modulus does not have too many differences under thermal cycle test and four-point-bend test. However FC specimen will have a clearly larger initial modulus in pure mechanical loading condition than thermal cycle condition. This observation indicates that in compression when the cracks and pores in coating closed, HOSP powder coating does not affected by the loading condition that much while FC coating is seriously influenced by the loading method. These characters of coatings under four-point-bend test will be helpful for optimal design and control of performance of thermo-mechanical coatings. The detail explanation of the coatings different performance under pure bending test and thermal cycle test requires further study.

7. Discussions

In the present study, a novel method to estimate the nonlinear elastic properties of TS ceramic coating is proposed and examined closely. The nonlinear stress-strain relation of the TS coating is generated by the micro cracks and pores embedded in the coating. A constitutive model was proposed which requires minimum unknown parameters to describe the nonlinear stress-strain relation. Under four-point-bend test, the moment-curvature relation was recorded and used to estimate unknown parameters by processing inverse analysis (Kalman filter). To perform the inverse analysis, a nonlinear bi-material beam solution was derived. By carry out iterative calculations, the relations between stress-strain and moment-curvature was established, which was used to estimated the unknown parameters.

After that, a close verification study using finite element method was carried out to exam the accuracy and the robustness of the proposed procedure. From the comparison of the re-constructed stress-strain relation with the original relation, a slight difference between the estimated curve and exact curve was observed. However, since the estimated always shows more compliance when the coating is under tensile stress, the estimated result can guarantee a safety condition. Furthermore, the factors might cause errors of the estimation (measurement errors, selection of transitional moment, calculation of initial modulus, and variation of axial stress through coating thickness) were discussed. The study demonstrated the proposed procedure can maintain robust with small measurement errors and slight differenced of the selection of transitional moment. However, since the calculation of the initial modulus is sensitive to the substrate thickness, substrate modulus and linear slope, the precision of the measurement of these parameters are highly required. Also, since axial stress through coating thickness has a great variation, the approximation of using mid-plane modulus might result in estimated errors.

Finally, experimental moment-curvature records of HOSP specimens and FC specimens were processed to estimate the nonlinear properties. Although it is impossible to prove the estimation is correct or not, the re-construction of the moment-curvature relation can demonstrate the usefulness of the proposed procedure. The estimated results

show that FC specimens have stiffer mechanical response under four-point-bend test than HOSP specimens. And it is caused by the difference of microstructures between the specimens. At last, a comparison of the properties from four-point-bend test and thermal cycle test was given out. The results show that YSZ coating have small nonlinearity and stiffer behavior under four-point-bend test. The boundary affection and the mechanical loading condition result in this significantly difference. And more tests needed to be carried out the exam this phenomenon.

References

Basu, D., Funke, C. and Steinbrech, R.W. 1999. Effect of Heat Treatment on Elastic Properties of Separated Thermal Barrier Coatings. J. Mater. Res., 14(12), pp. 4643-50.

Carlotti, G., Doucet, L., Dupeux, M., 1997. Elastic properties of silicon dioxide films deposited by chemical vapour deposition from tetraethylorthosilicate. Thin Solid Films 296, 102–105.

Eldridge, J.I., Morscher, G.N. and Choi, S.R. 2002. Quasistatic vs. Dynamic Modulus Measurements of Plasma Sprayed Thermal Barrier Coatings. Ceram. Eng. Sci. Proc., 23, pp. 371-80.

Harok, V., Neufuss, K., 2001. Elastic and inelastic effects in compression in plasma-sprayed ceramic coatings. Journal of Thermal Spray Technology 10 (1), 126–132.

Hunsche, B., Vergo¨ hl, M., Neuha¨user, H., Klose, F., Szyszka, B., Matthe´e, T., 2001. Effect of deposition parameters on optical and mechanical properties of MF- and DC-sputtered Nb2O5 films. Thin Solid Films 392 (2), 184–190.

Kesler, O., Matejicek, J., Sampath, S., Suresh, S., Gnaeupel-Herold, T., Brand, P.C., Prask, H.J., 1998. Measurement of residual stress in plasma-sprayed metallic, ceramic and composite coatings. Materials Science and Engineering A 257, 215–224.

Kim, S.R. and Nairn, J.A. 2000. Eng. Frac. Mech. **65,** 573.

Kroupa, F., Dubsky, J., 1999. Pressure dependence of Young's moduli of thermal sprayed materials. Scripta Materialia 40 (11), 1249–1254.

Kroupa, F., Plesek, J., 2001. Bending of beams with elastically non-liner coatings. Journal of Thermal Spray Technology Volume 11(4), 508 – 516.

Kroupa, F., Plesek, J., 2002. Nonlinear elastic behavior in compression of thermally sprayed materials. Materials Science and Engineering A 328, 1–7.

Krulevitch, P., Ramsey, P.B., Makowiecki, D.M., Lee, A.P., Northrup, M.A., Johnson, G.C., 1996. Mixed-sputter deposition of Ni–Ti–Cu shape memory films. Thin Solid Films 274, 101–105.

Kucuk, A., Berndt, C.C., Senturk, U., Lima, R.S. and Lima, C.R.C. 2000 Influence of Plasma Spray Parameters on Mechanical Properties of Yttria Stabilized Zirconia Coatings: Four Point Bending Test. Mater. Sci. Eng. A.,284, pp. 29-40.

Kuroda, S., Fukushima, T., Kitahara, S., 1988. Simultaneous measurement of coating thickness and deposition stress during thermal spraying. Thin Solid Films 164, 157–163.

Kuroda, S., Fukushima, T., Kitahara, S., 1990. Generation mechanisms of residual stresses in plasma-sprayed coatings. Vacuum 41, 1297–1299.

Lacquaniti, V., Monticone, E., Picotto, G.B., 1997. Structural and surface properties of sputtered Nb films for multilayer devices. Surface Science 377–379, 1042–1045.

Liu. Y, et al., Non-linear elastic properties of plasma-sprayed zirconia coatings and associated relationships with processing conditions, Acta Mater (2007), doi:10.1016/ j.actamat. 2007. 04.037

Liu. Y, et al., Anelastic Behavior of Plasma-Sprayed Zirconia Coatings, J. Am. Ceram. Soc., 91 [12] 4036–4043 (2008) DOI: 10.1111/j.1551-2916.2008.02789.x

Matejicek, J., Sampath, S., Gilmore, D., Neiser, R., 2003. In situ measurement of residual stresses and elastic moduli in thermal sprayed coatings: Part 2: processing effects on properties of Mo coatings. Acta Materialia 51, 873–885.

Menzel, S., Strehle, S., Wendrock, H., Wetzig, K., 2005. Effect of Ag-alloying addition on the stress–temperature behavior of electroplated copper thin films. Applied Surface Science 252, 211–214.

Nakamura, T., Liu, Y. 2006. Determination of nonlinear properties of thermal sprayed ceramic coatings via inverse analysis. International Journal of Solids and Structures 44 (2007) 1990–2009.

Nohava, J., Kroupa. F. 2005. Nonlinear stress-strain behavior of plasma sprayed ceramic coatings. Acta technica ČSAV, vol. 50, n°3, pp. 251-262

Oka, Y., Tao, M., Nishimura, Y., Azuma, K., Fujiwara, E., Yatsuzuka, M., 2003. Properties of thick DLC films prepared by plasmabased ion implantation and deposition using combined RF and H.V. pulses. Nuclear Instruments and Methods in Physics Research B 206, 700–703.

Steinbrech, R.W. 2002. Thermomechanical Behavior of Plasma Sprayed Thermal Barrier Coatings. Ceram. Eng. Sci. Proc., 23, pp. 379- 408.

Stoney, G., 1909. The tension of metallic films deposited by electrolysis. Proc Roy Soc London A 82, 172–175.

Tsui, Y.C., Clyne, T.W., 1997. An analytical model for predicting residual stresses in progressively deposited coatings: Part 1: planar geometry. Thin Solid Films 306, 23–33.

Waki, H., Ogura, K., Nishikawa, I., Ohmori, A., 2004. Monotonic and cyclic deformation behavior of plasma-sprayed coatings under uniaxial compressive loading. Materials Science and Engineering A 374, 129–136.

Wang, W., Li, C., Wang, Y., Yang, G., Sonoya, K., 2006. Tensile deformation behavior of plasma-sprayed Ni–45Cr coatings. Surface and Coatings Technology 201, 842–847.

Appendix

Determination of curvature of the beam from deflection

Figure 32 shows a schematic diagram of four-point-bend test. The inner loading span is *l*, and the outer loading span is *a*. ν is the deflection of between the inner span. Suppose at some time the loading force is *P*, then from beam theory solution, the deflection of the beam is:

$$v(x) = -\frac{Pa(a^2 - 6ax - 3lx + 3x^2)}{6EI}, \text{ where } a \le x \le a + l \tag{A.1}$$

Then the curvature can be computed as:

$$\kappa = \left|\frac{d^2v}{dx^2}\right| = \left|\frac{d^2}{dx^2}\left[-\frac{Pa(a^2 - 6ax - 3lx + 3x^2)}{6EI}\right]\right| = \frac{Pa}{EI} \tag{A.2}$$

So curvature is a constant within the inner loading indenter.

The deflection of the midpoint is:

$$v = -\frac{Pa}{24EI}(8a^2 + 12al + 3l^2) \tag{A.3}$$

And the curvature at midpoint is:

$$\kappa = \frac{Pa}{EI} = -\frac{24v}{(8a^2 + 12al + 3l^2)} \tag{A.4}$$

Determination of the relation between axial strain and curvature with initial curvature

The initial axial stress can be considered as the combination of two behaviors: the mismatch in length of the substrate and TS coating after the fabrication process and the initial curvature developed by the mismatch force. Figure 33 explains the combination of these two contributions. Suppose at the fabrication process, the substrate is heated up and extends to the length *L**, and at this time, the coating is sprayed onto the substrate. After the fabrication, the beam cools down to the room temperature. Suppose the substrate and the coating will shrink to the length $L - L_0$ and *L*, respectively (generally, the coefficient of the thermal expansion of the substrate is larger than the ceramic coating).

Since the coating and the substrate are bonded together, the substrate will be stretched to a length $L - L_0 + \delta_S$, while coating will be compressed to a length $L - \delta_c$, where $\delta_C + \delta_S = L_0$. The mismatch in length will generate compressive internal stresses within the coating. Then the following equations can be written:

$$\frac{\delta_C}{L} = \frac{F_{mis}}{E_C A_C}, \quad \frac{\delta_S}{L - L_0} = \frac{F_{mis}}{E_S A_S} \tag{A.5}$$

Here, $A_C(=tb), A_S(=hb)$ are the intersection area of the coating and substrate, respectively. E_C, E_S are the Young's modulus of the coating and substrate at room temperature, respectively. Then the mismatch force and axial stress can be expressed as:

$$F_{mis} = \frac{L_0 E_C E_S A_C A_S}{L E_S A_S + (L - L_0) E_C A_C} \tag{A.6}$$

$$\varepsilon_C^{mis} = -\frac{\delta_C}{L} = -\frac{F_{mis}}{E_C A_C} = \frac{L_0 E_S A_S}{L E_S A_S + (L - L_0) E_C A_C} \tag{A.7}$$

However, since the mismatch force will cause an internal moment, the beam will have an initial curvature, with related the thickness of the beam. Suppose the mismatch forces are loaded at the centers of the coating and substrate layers, the internal moment can be expressed as:

$$M_i = F_{mis}\left(\frac{t+h}{2}\right) \tag{A.8}$$

As discussed above, the curvature-moment relation is $\kappa = M / I_E$. Here, since coating is linear elastic at the room temperature, the stiffness and the neutral axes can be written as:

$$I_E = \frac{E_S{}^2 h^4 + E_C{}^2 t^4 + 2E_S E_C ht\left(2h^2 + 3ht + 2t^2\right)}{12\left(E_S h + E_C t\right)} \tag{A.9}$$

$$y_0 = \frac{E_S h^2 + E_C t^2 + 2E_C ht}{2(E_S h + E_C t)} \tag{A.10}$$

Here, E_C is the Young's modulus of the coating at the room temperature. The strain generated by the initial curvature is:

$$\varepsilon_K = -\kappa_0 (y - y_0) = \frac{L_0 E_C E_S ht}{L E_S h + (L - L_0) E_C t} \cdot \frac{t+h}{2} \cdot \frac{12\left(E_S h + E_C t\right)}{E_S{}^2 h^4 + E_C{}^2 t^4 + 2E_S E_C ht\left(2h^2 + 3ht + 2t^2\right)} (y - y_0) \tag{A.11}$$

The total strain in the coating should be the combination of these two kinds of strains:

$$\varepsilon_C = \frac{L_0 E_S h}{L E_S h + (L - L_0) E_C t} + \frac{L_0 E_C E_S ht}{L E_S h + (L - L_0) E_C t} \cdot \frac{t+h}{2} \cdot \frac{12\left(E_S h + E_C t\right)}{E_S{}^2 h^4 + E_C{}^2 t^4 + 2E_S E_C ht\left(2h^2 + 3ht + 2t^2\right)} (y - y_0) \tag{A.12}$$

Noted that κ_0 is the curvature introduced by the mismatch force when the external moment is zero. So the initial curvature and mismatch force have the following relation:

$$\kappa_0 = \frac{L_0 E_C E_S ht}{L E_S h + (L - L_0) E_C t} \cdot \frac{t+h}{2} \cdot \frac{1}{I_E} \tag{A.13}$$

With these relations, the mismatch length L_0 can be computed, and the axial stress in the coating can be expressed in terms of initial curvature and total curvature:

$$\varepsilon_C = \frac{2 I_E \kappa_0}{E_C t (h + t)} - \kappa (y - y_0) \tag{A.14}$$

Here, κ is total curvature measured by the laser.

Determination of average secant modulus through-thickness

In terms of σ^* and ε^* in equation (2), the average secant modulus is expressed as:

$$E^*_{ave} = \frac{\sigma^*}{\varepsilon^*} = \begin{cases} E_C, & \sigma^* < 0 \\ \dfrac{E_C \sigma_N^{n-1}}{\sigma_N^{n-1} + (\sigma^*)^{n-1}}, & \sigma^* > 0 \end{cases} \tag{A.15}$$

Suppose ε, E_C, σ_N and n are known, Newton's method can be used to determine σ^* for a given ε^* under $\sigma^* > 0$.
First an implicit function is defined as

$$f(\sigma^*) = \frac{\sigma^*}{E_C} + \frac{(\sigma^*)^n}{E_C \sigma_N^{n-1}} - \varepsilon^* = 0 \tag{A.16}$$

Then the following iteration is carried out to determine σ^*

$$\sigma^*_i = \sigma^*_{i-1} - \frac{f(\sigma^*_{i-1})}{f'(\sigma^*_{i-1})}, \quad \text{where} \quad f'(\sigma^*_{i-1}) = \frac{1}{E_C}\left[1 + n\left(\frac{\sigma^*_{i-1}}{\sigma_N}\right)^{n-1}\right] \tag{A.17}$$

The convergence is satisfied when $\left|\sigma^*_i - \sigma^*_{i-1}\right| < 1\times10^{-4}$. Then (A.11) is used to compute E^*_{ave}.

Determination of transitional and residual stress

The strain can be expressed as:

$$\varepsilon = \begin{cases} \dfrac{\sigma}{E} - \dfrac{|\sigma_T|^n}{E\sigma_N^{n-1}} & \sigma < \sigma_T \\ \dfrac{\sigma}{E} + \dfrac{(\sigma - \sigma_T)^n - |\sigma_T|^n}{E\sigma_N^{n-1}} & \sigma \geq \sigma_T \end{cases} \tag{A.18}$$

When the stress is equal to transitional stress, the transitional strain is:

$$\varepsilon_T = \frac{\sigma_T}{E} - \frac{|\sigma_T|^n}{E\sigma_N^{n-1}} \tag{A.19}$$

Figure 34 plots a typical stress-strain relation. Initial point and transitional point is marked as A and C. The strain at point A is :

$$\varepsilon_R = \frac{2I^*_E \kappa_A}{E^* t(t+h)} - \kappa_A (y - y^*_0) \tag{A.20}$$

Because from point A to point C it is linear part, so

$$\varepsilon_R = \varepsilon_C - (\kappa_A - \kappa_C)(y - y_0) \tag{A.21}$$

And the stress relation is:

$$\sigma_A = \sigma_C + E(\varepsilon_A - \varepsilon_C) \tag{A.22}$$

Then the secant modulus at point A is:

$$E_A^* = \frac{\sigma_R}{\varepsilon_R} = \frac{\sigma_T + E\left[-(\kappa_A - \kappa_C)(y - y_0)\right]}{\frac{\sigma_T}{E} - \frac{|\sigma_T|^n}{E\sigma_N^{n-1}} - (\kappa_A - \kappa_C)(y - y_0)} \tag{A.23}$$

Then strain at point A is:

$$\frac{\sigma_T}{E} - \frac{|\sigma_T|^n}{E\sigma_N^{n-1}} - (\kappa_A - \kappa_C)(y - y_0) = \frac{2I_E^*\kappa_A}{E^* t(t+h)} - \kappa_A(y - y_0^*) \tag{A.24}$$

Where

$$I_E^* = \frac{{E_S}^2 h^4 + (E_A^*)^2 t^4 + 2E_S E_A^* ht\left(2h^2 + 3ht + 2t^2\right)}{12\left(E_S h + E_A^* t\right)} \tag{A.25}$$

$$y_0^* = \frac{E_S h^2 + E_A^* t^2 + 2E_A^* ht}{2(E_S h + E_A^* t)} \tag{A.26}$$

Because the transitional stress is negative, so the implicit function used in secant method is:

$$f(\sigma_T) = \frac{\sigma_T}{E} - \frac{(-\sigma_T)^n}{E\sigma_N^{n-1}} - (\kappa_A - \kappa_C)(y - y_0) - \frac{2I_E^*\kappa_A}{E^* t(t+h)} + \kappa_A(y - y_0^*) \tag{A.27}$$

The iteration steps are shown below:

$$(\sigma_T)_i = (\sigma_T)_{i-1} - f\left[(\sigma_T)_{i-1}\right]\frac{(\sigma_T)_{i-1} - (\sigma_T)_{i-2}}{f\left[(\sigma_T)_{i-1}\right] - f\left[(\sigma_T)_{i-2}\right]} \tag{A.28}$$

The convergence is satisfied when $\left|(\sigma_T)_i - (\sigma_T)_{i-1}\right| < 1\times10^{-3}$. Once transitional stress σ_T is calculated, the residual stress σ_R can be computed.

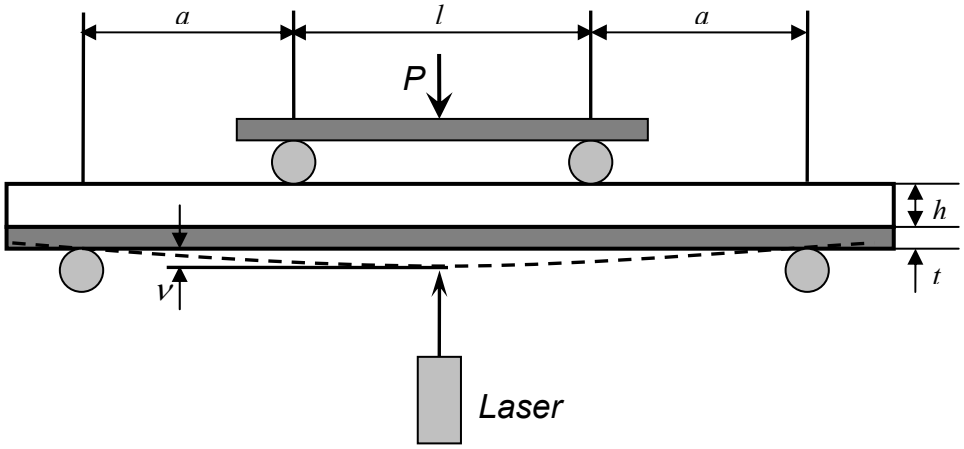

Figure 1. Schematic diagram of four-point-bend test. *P* is the force generated by the indenter to add moment. The inner span is *l*, and outer span is *a*. *v* is the deformation of the midpoint of the beam measured by laser.

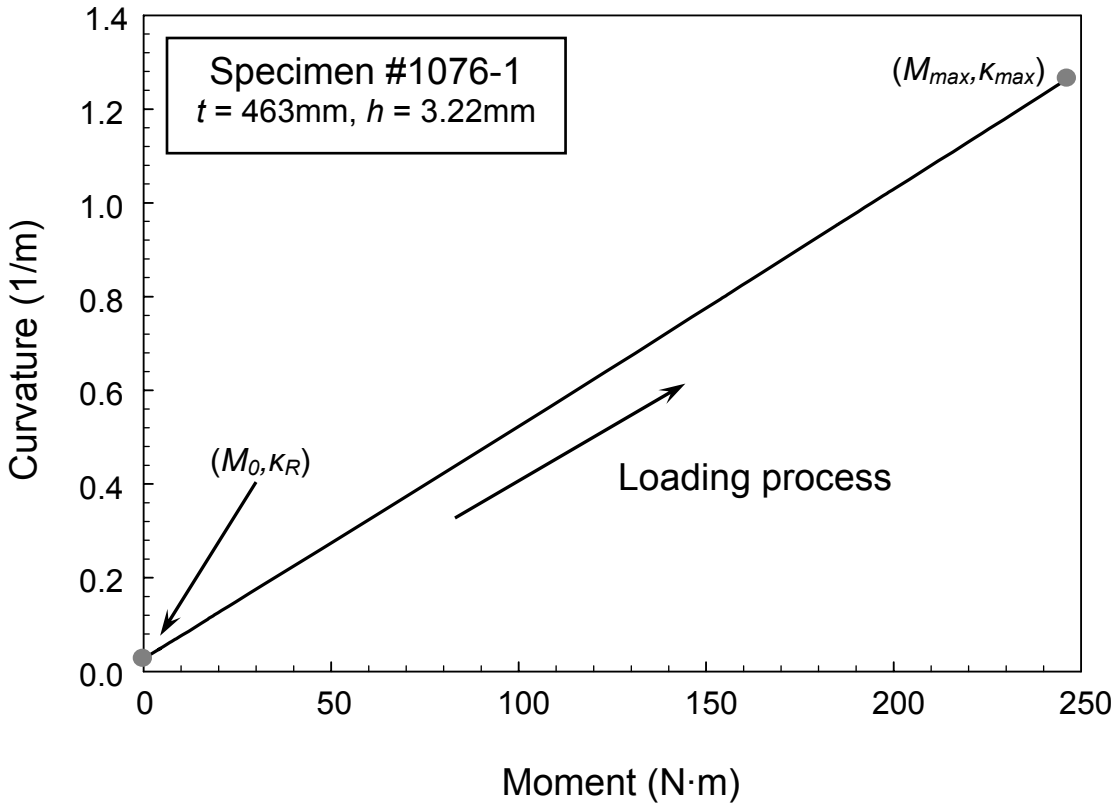

Figure 2. Experimental measured moment-curvature relation of YSZ TS coating on Al substrate during loading process.

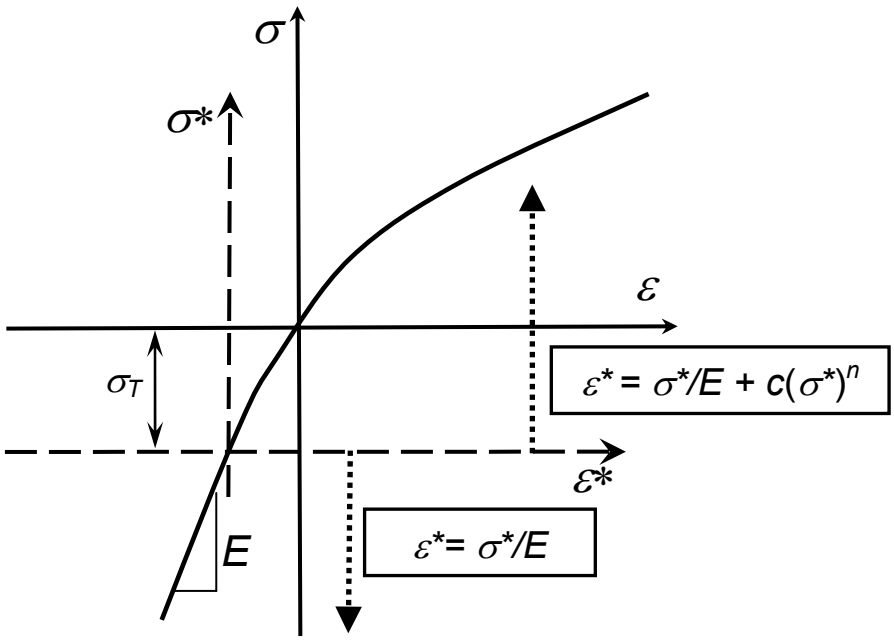

Figure 3. Nonlinear stress-strain relation model for TS ceramic coatings. Change in linear and nonlinear stress-strain relation occurs at transitional stress σ_T. Corresponding equations are noted below and above the ε^* axis, respectively.

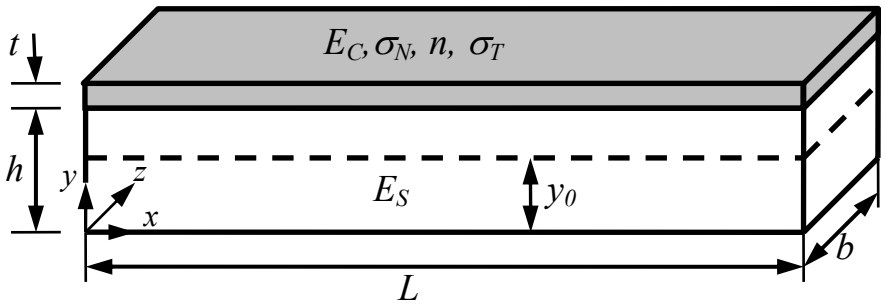

Figure 4. Schematic of TS coating on substrate with relevant dimensions. Corresponding material parameters are noted and the location of neutral axis y_o is shown.

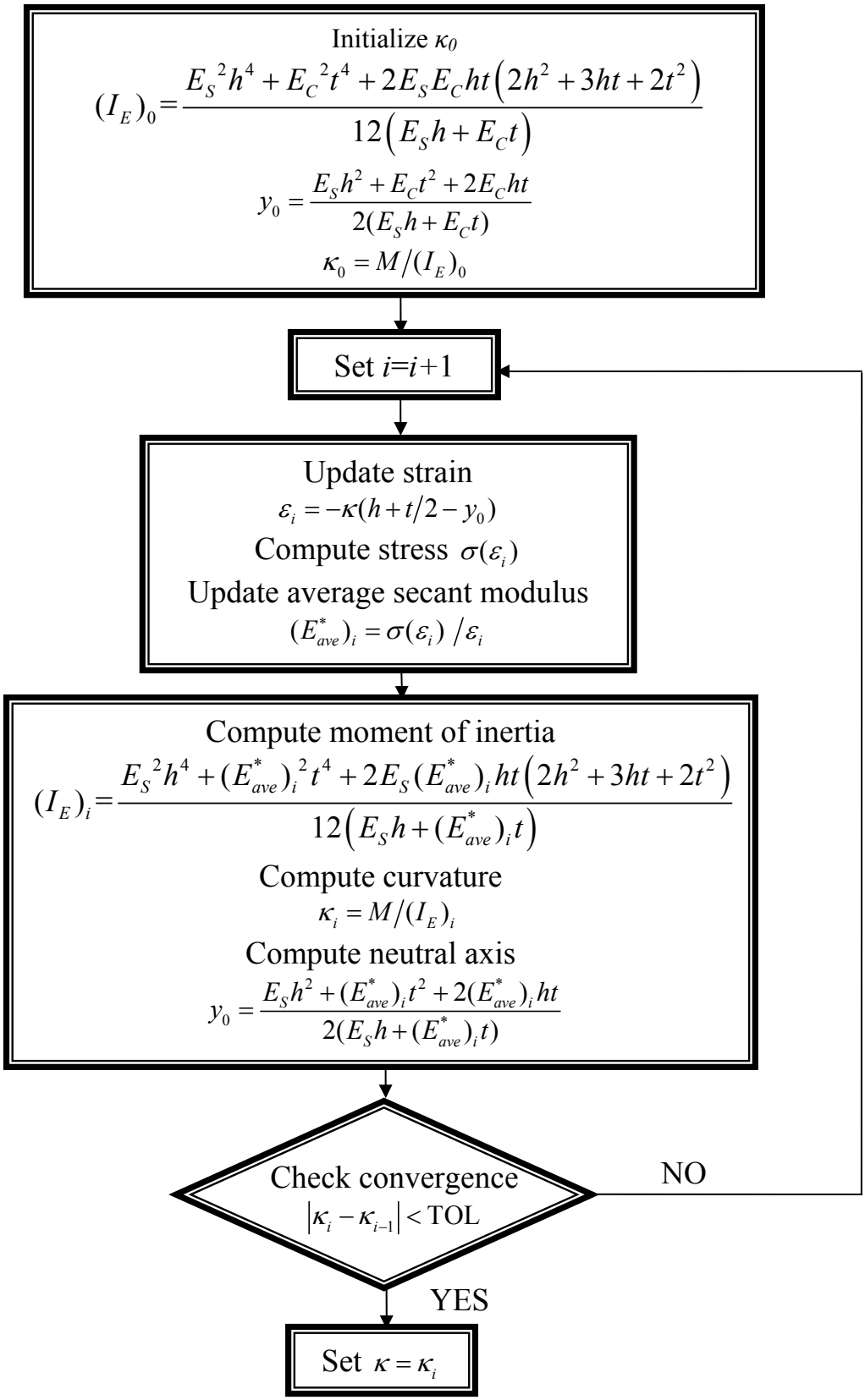

Figure 5. Flowchart to compute curvature change $\Delta\kappa$ for a given moment change ΔM.

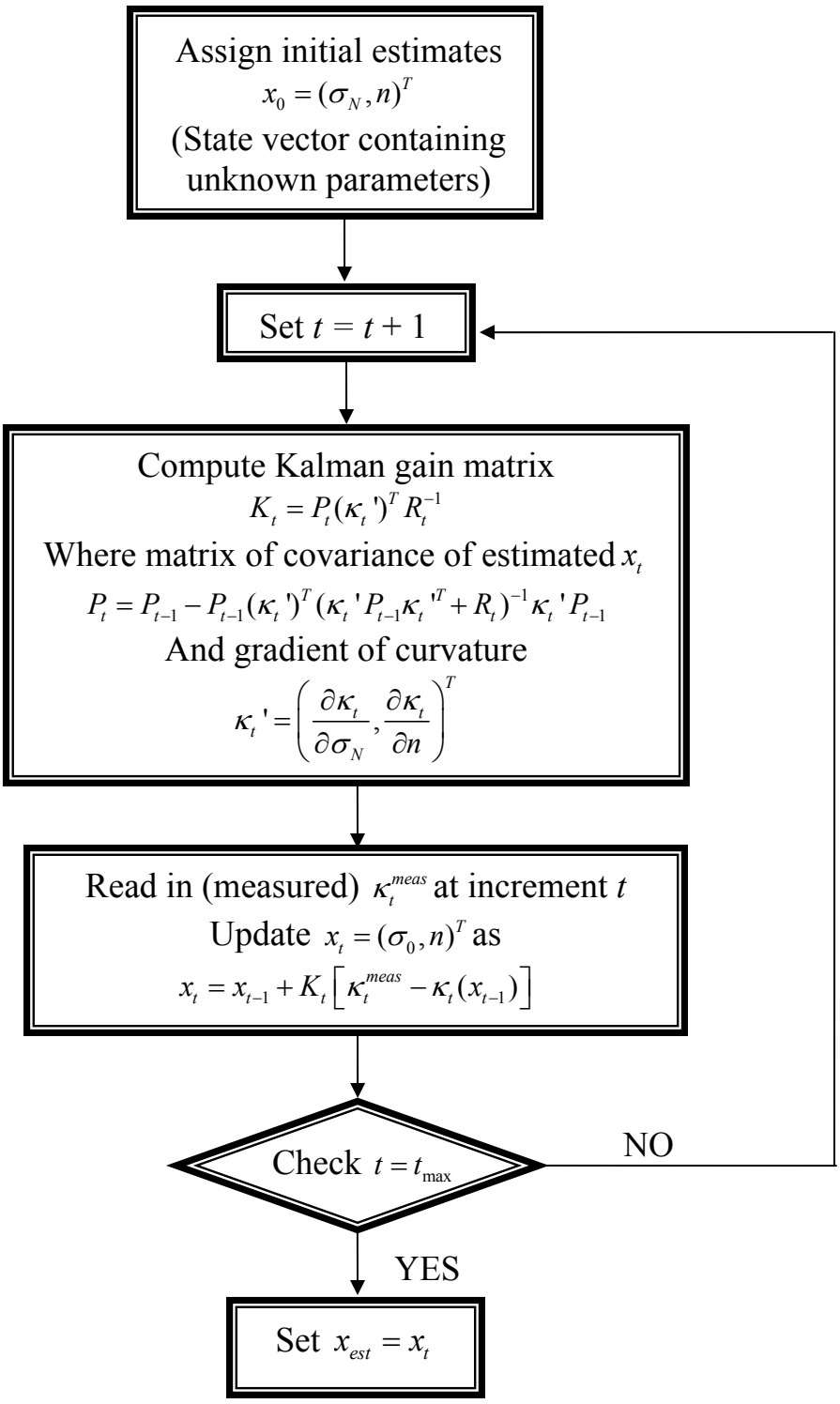

Figure 6. Flowchart of Kalman filter procedure to estimate the unknown parameters.

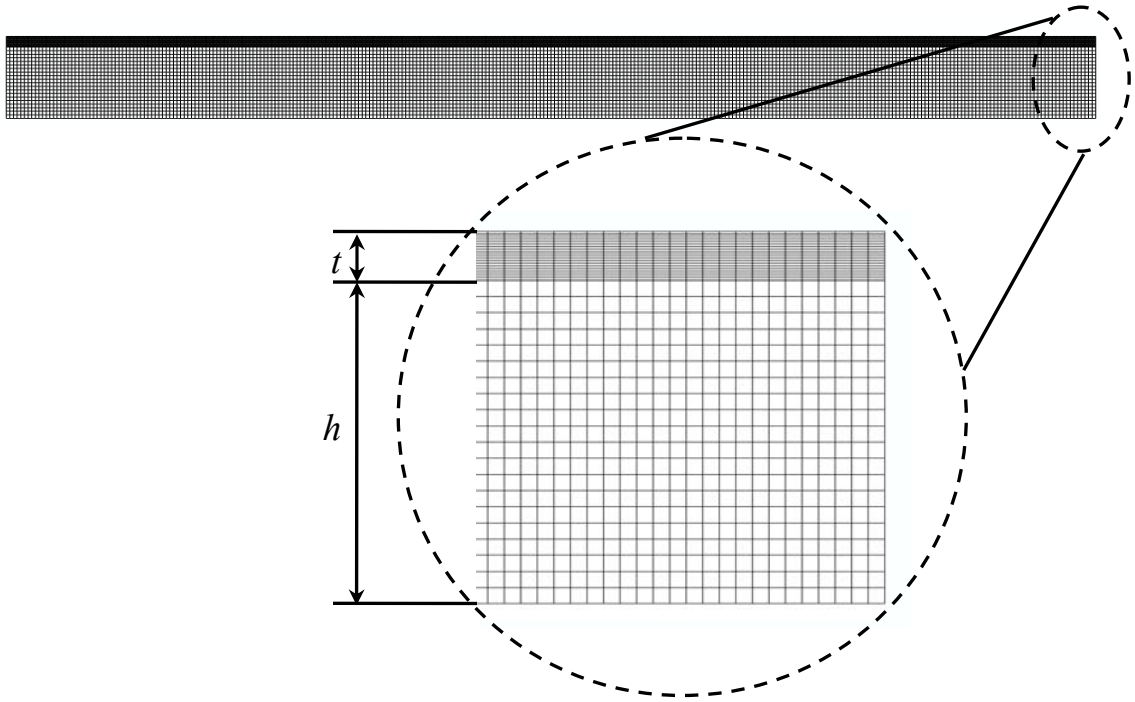

Figure 7. Finite element model of YSZ coating beam. 26700 elements are used in the model. Smaller elements are required for coatings to simulate the nonlinear properties and avoid inconsistent results in stress and strain.

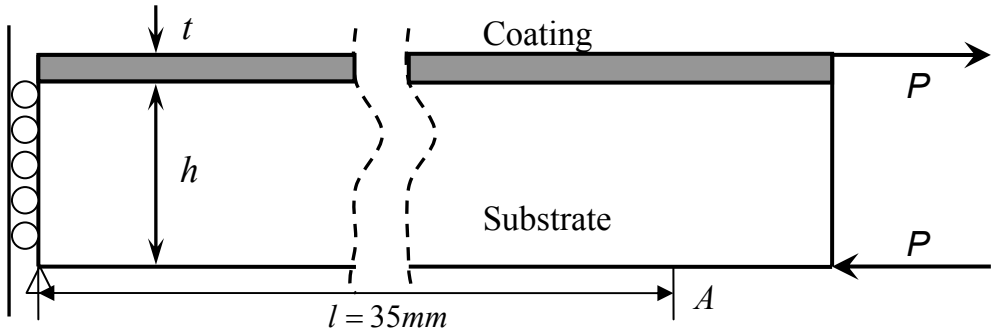

Figure 8. Schematic model of boundary and loading condition of the finite element model. *P* is the force added to generate moment. *A* is the point used to measure the deformation and calculate the curvature of the beam.

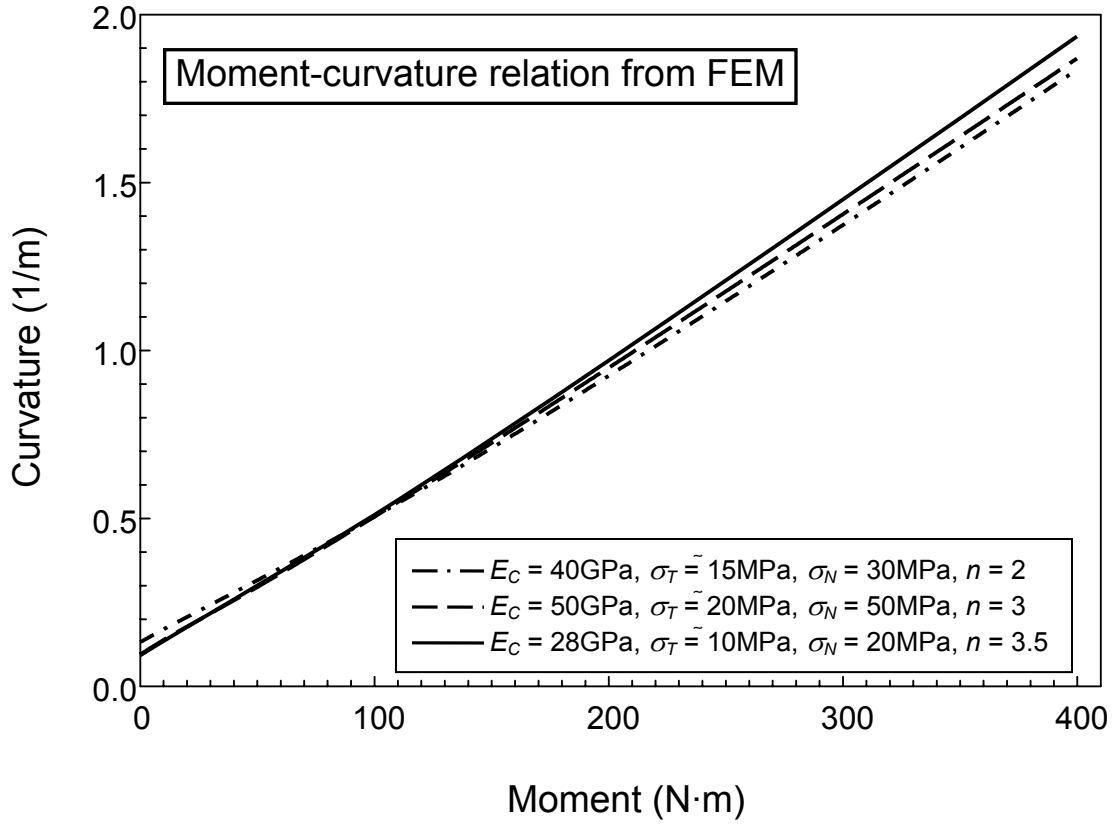

Figure 9. Moment-curvature relation from finite element method with different parameters input.

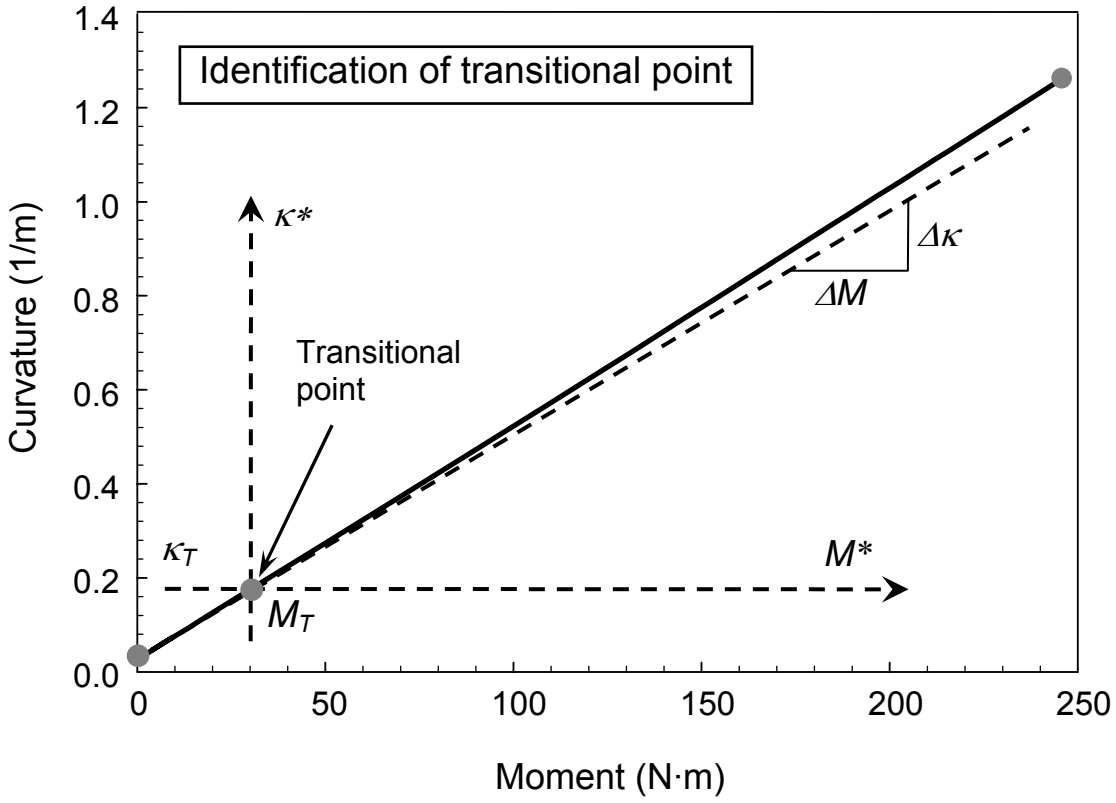

Figure 10. Identification of transitional point (linear to nonlinear) to extract initial tangent modulus E_c from ΔM and $\Delta\kappa$. Shifted coordinates centered at M_T and κ_T are also shown.

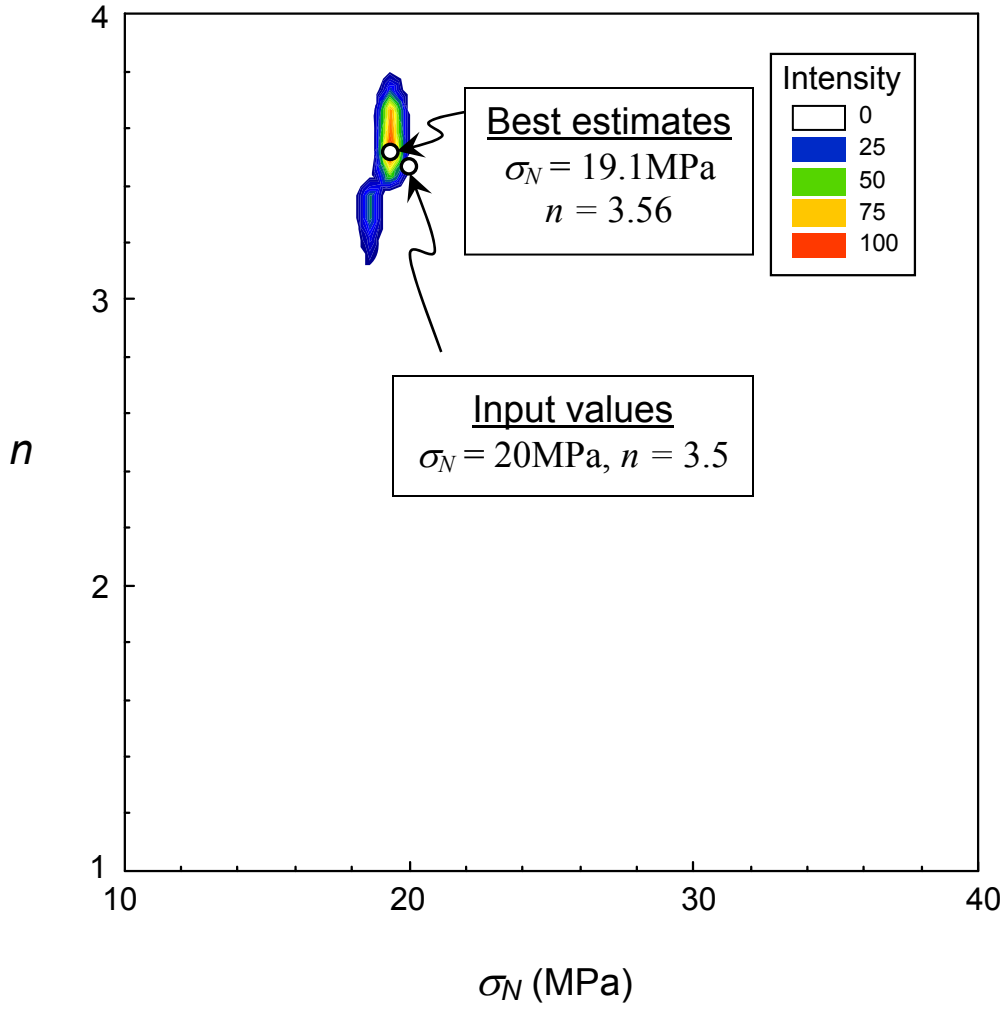

Figure 11. Intensity of convergence plot generated from the inverse analysis from simulated TS coating moment-curvature relation. A high intensity represents convergence of many initial estimates and likely location of best estimates. The scale of intensity (i.e., 0–100) is relative. The location of input values is also noted.

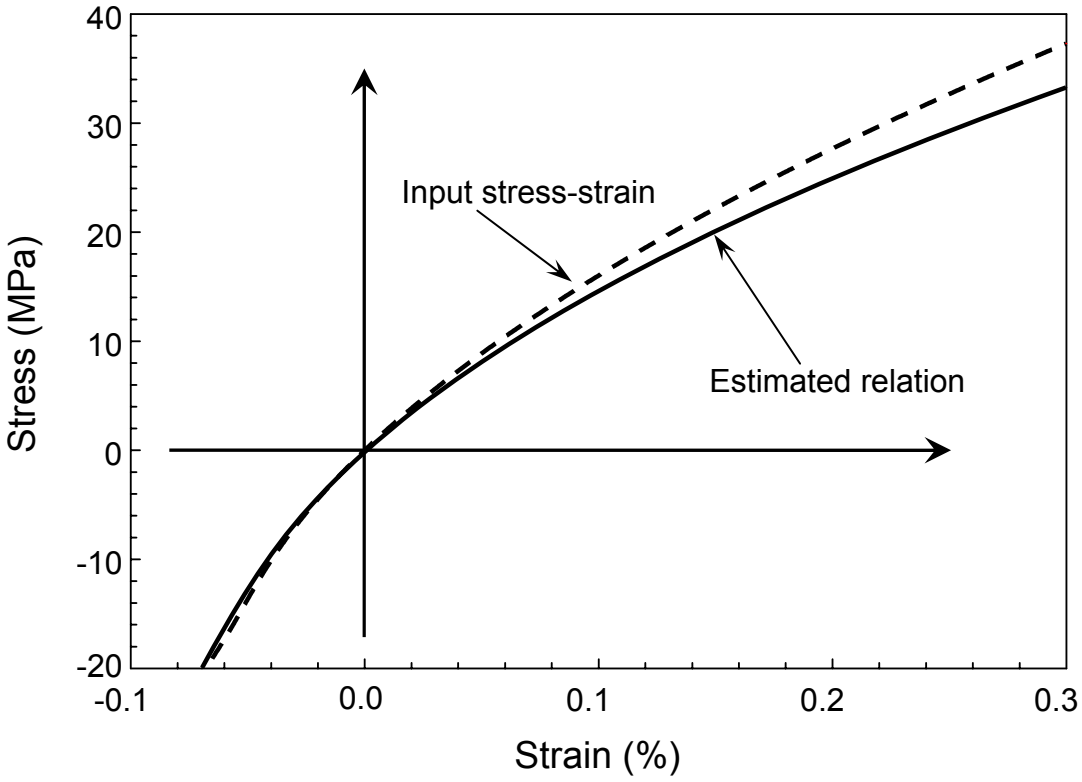

Figure 12. Comparison of input stress-strain relation and estimated relation from inverse analysis. Input is $\sigma_N = 20$MPa, $n = 3.5$, estimated is $\sigma_N = 19.3$MPa, $n = 3.56$.

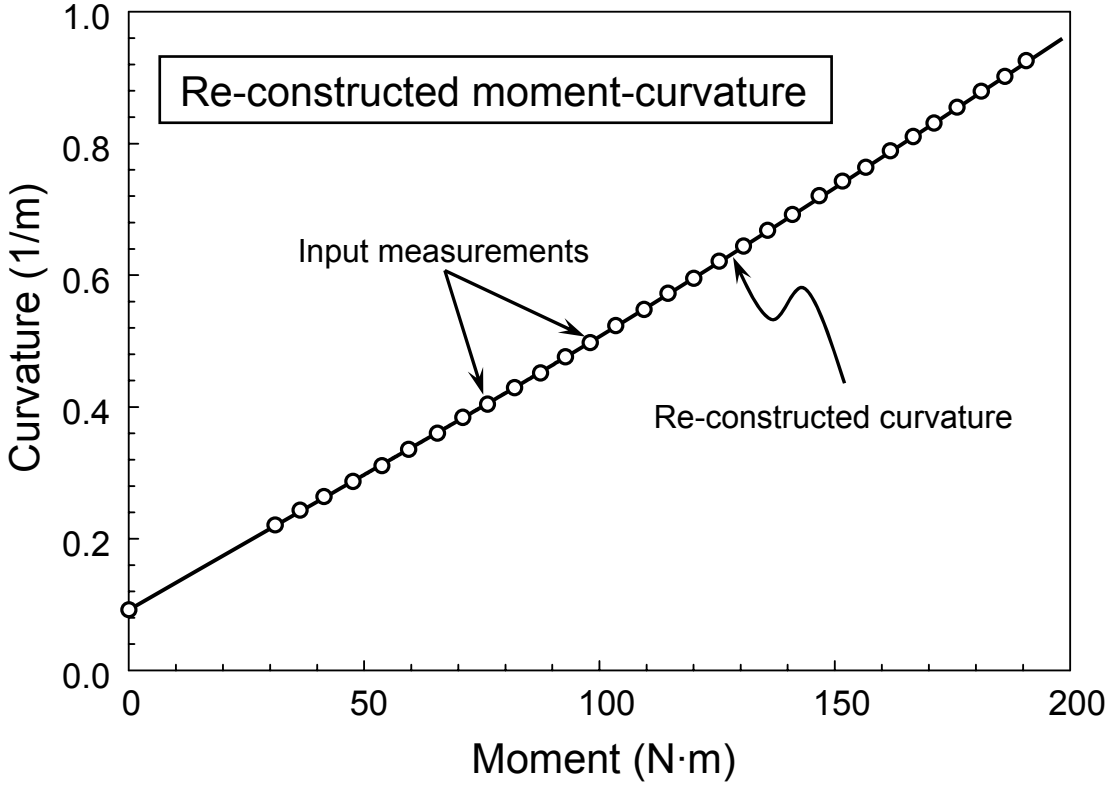

Figure 13. Comparison between input and estimated results obtained by assigning the best estimates as input properties in the nonlinear bi-material formula.

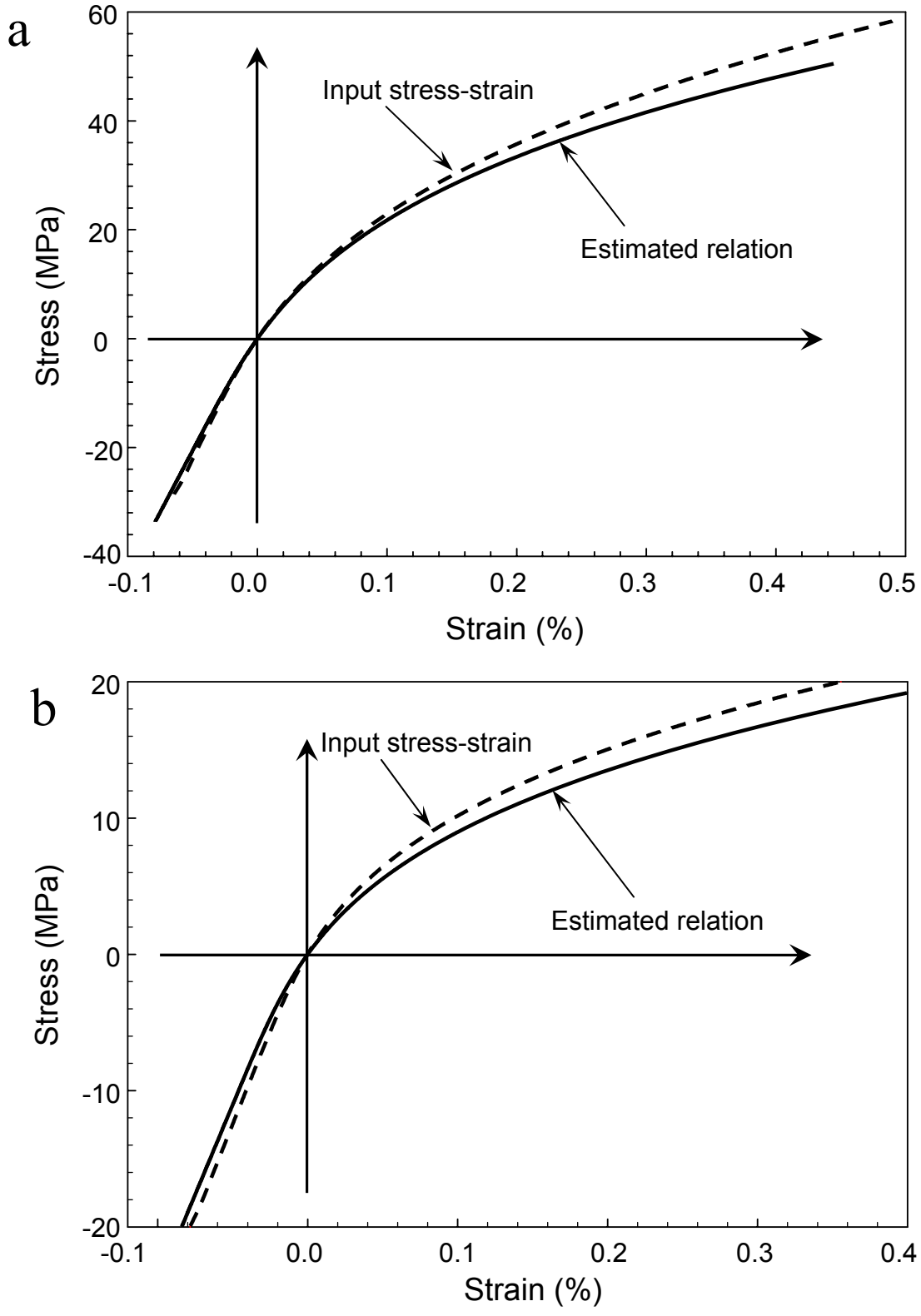

Figure 14. Comparison of input stress-strain relation and estimated relation from inverse analysis. (a) Input is $\sigma_N = 50$MPa, $n = 3$, estimated is $\sigma_N = 51.2$MPa, $n = 3.42$. (b) Input is $\sigma_N = 30$MPa, $n = 2$, estimated is σ_N=28.7MPa, $n = 2.19$.

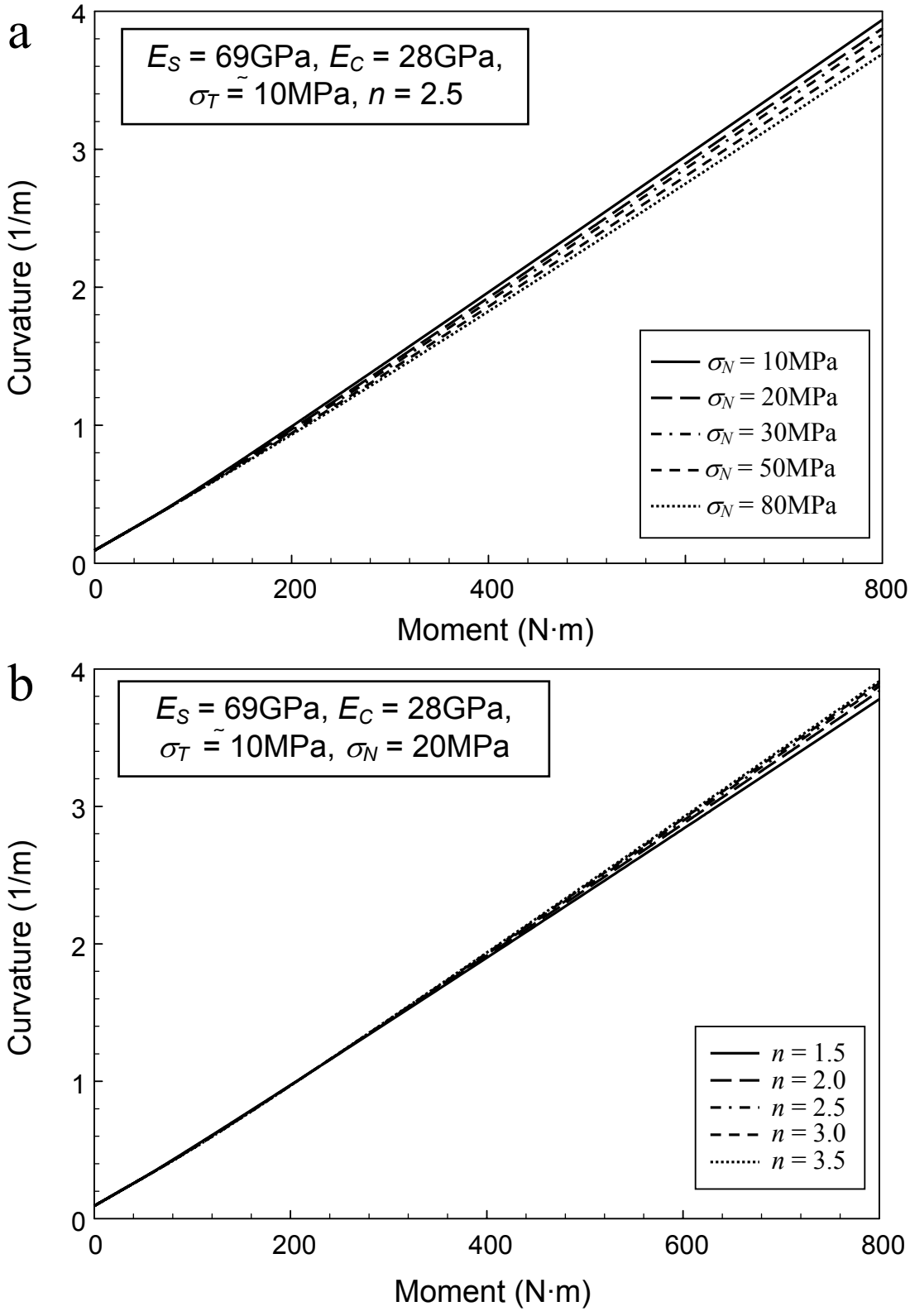

Figure 15. Simulated moment-curvature relation with different nonlinear parameters input. (a) Reference stresses vary from 10-80MPa. (b) Power-law exponents vary from 1.5-3.5.

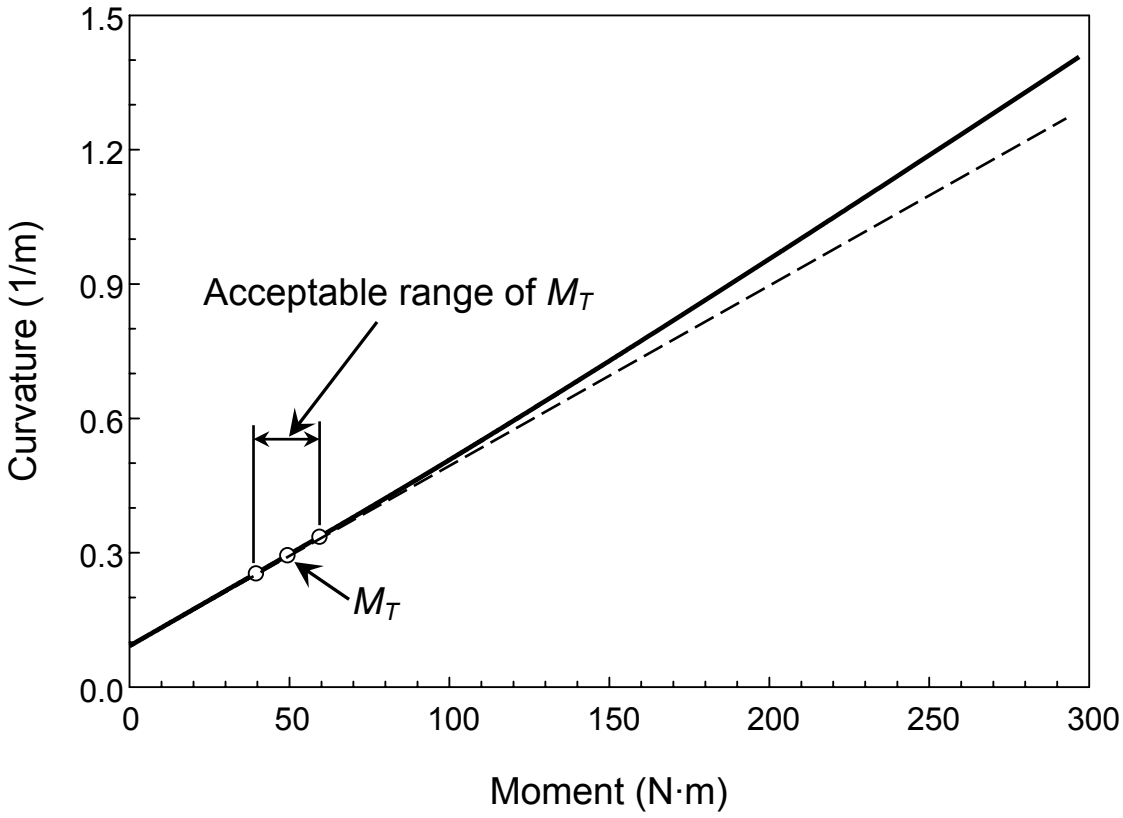

Figure 16. Acceptable selection range of transitional moment. The exact transitional moment is 50N·m. 40-60N·m is the acceptable range of transitional moment to guarantee a good estimation.

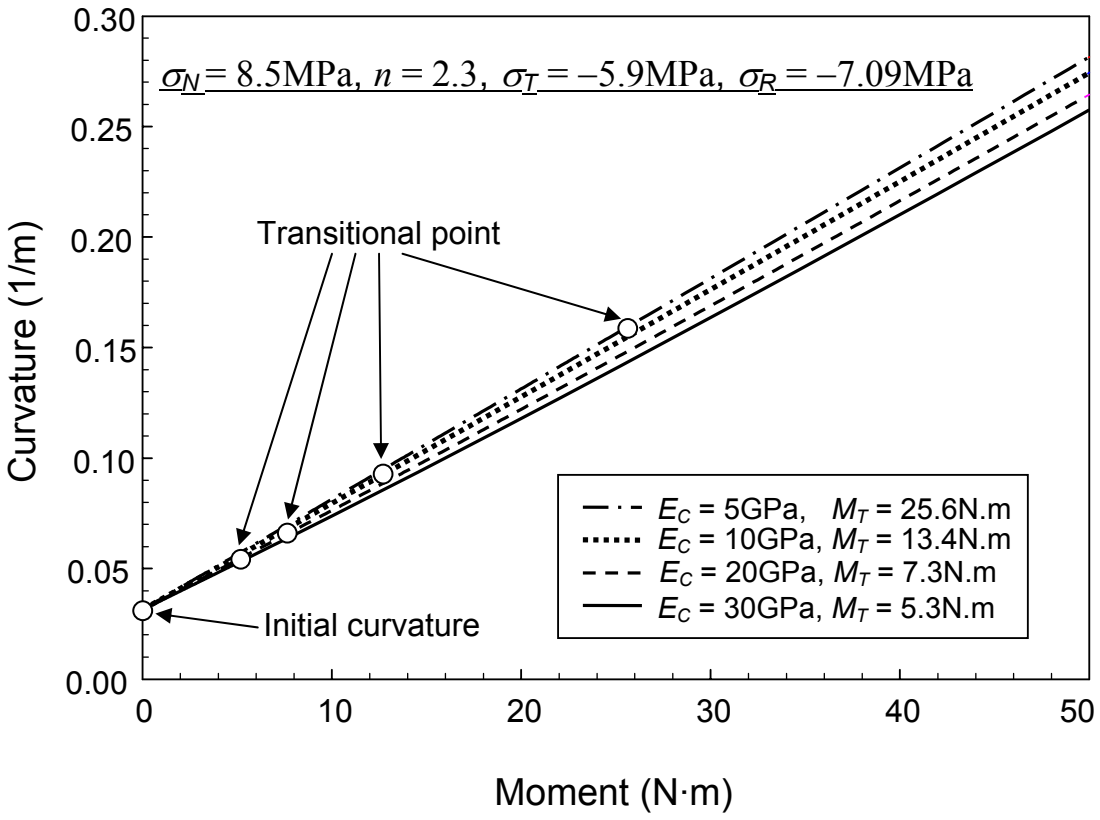

Figure 17. Transitional point according to different initial modulus. The linear slope between zero moment and transitional moment is used to calculate the initial modulus.

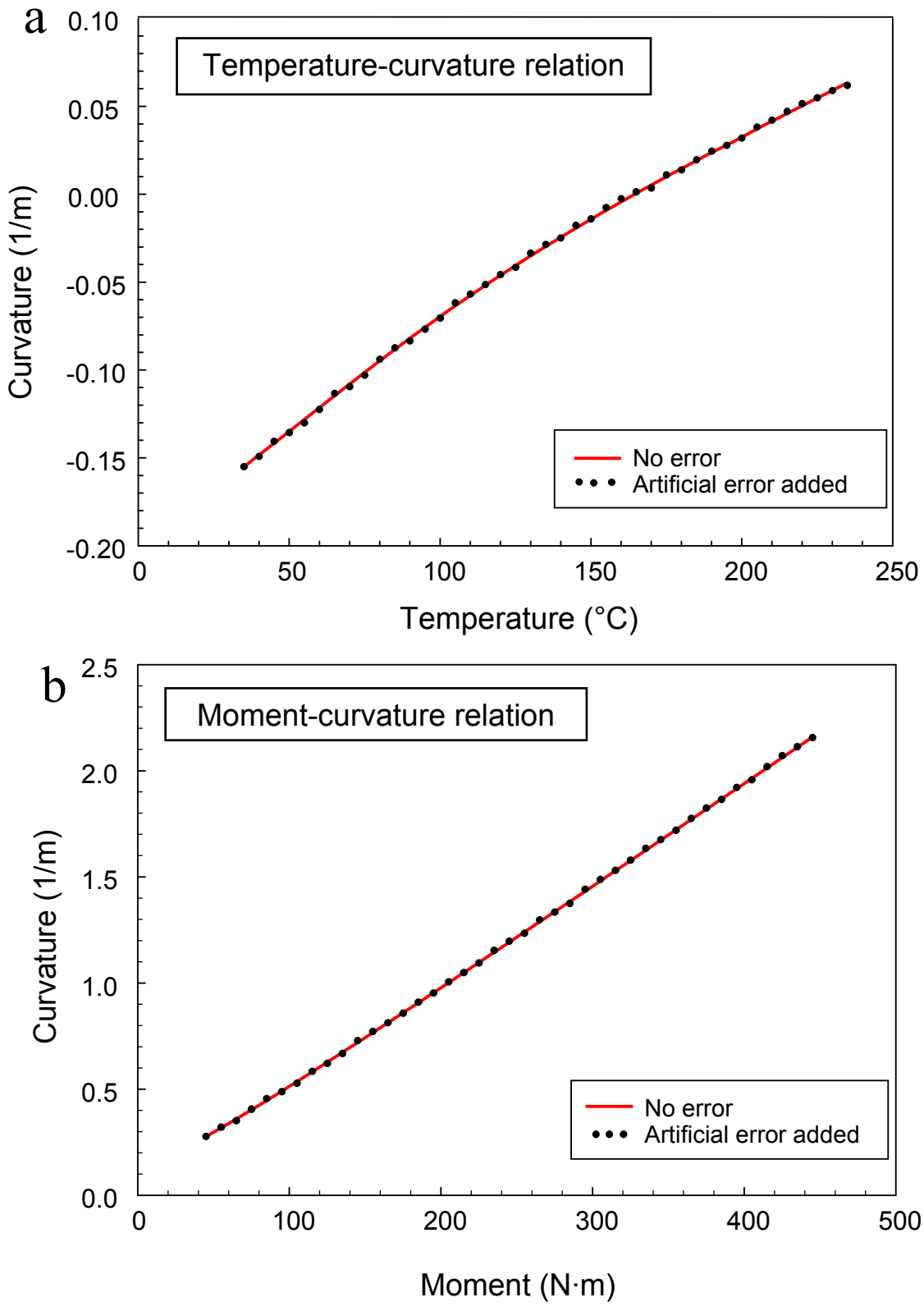

Figure 18. (a) Temperature-curvature record with artificial errors added to the nonlinear portion (error bounds ±0.002m^{-1}). (b) Moment-curvature record with artificial errors added to the nonlinear portion (error bounds ±0.106m^{-1}).

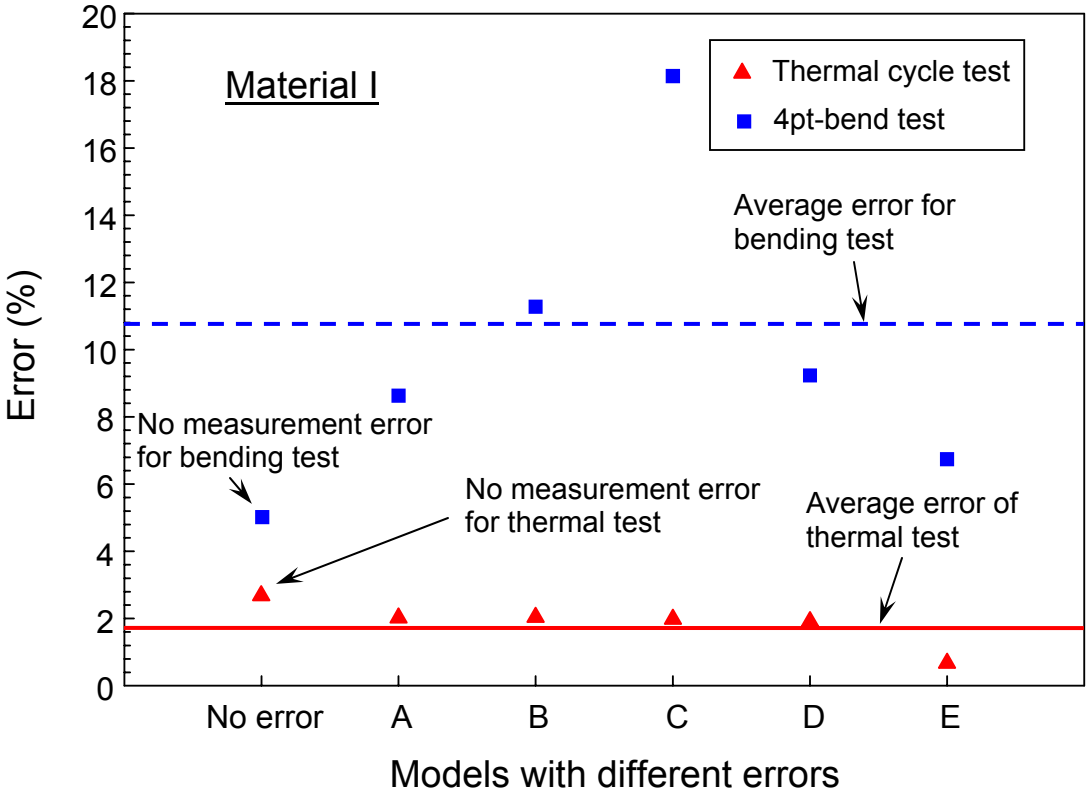

Figure 19. Estimated errors for material I (E = 31GPa, σ_N = 51MPa, n = 3.23, σ_T = −31MPa). Models A-E are random errors added to the no error input. Errors of the estimated parameters are plotted in dots. Horizontal lines are the average errors of estimated parameters from inverse analysis.

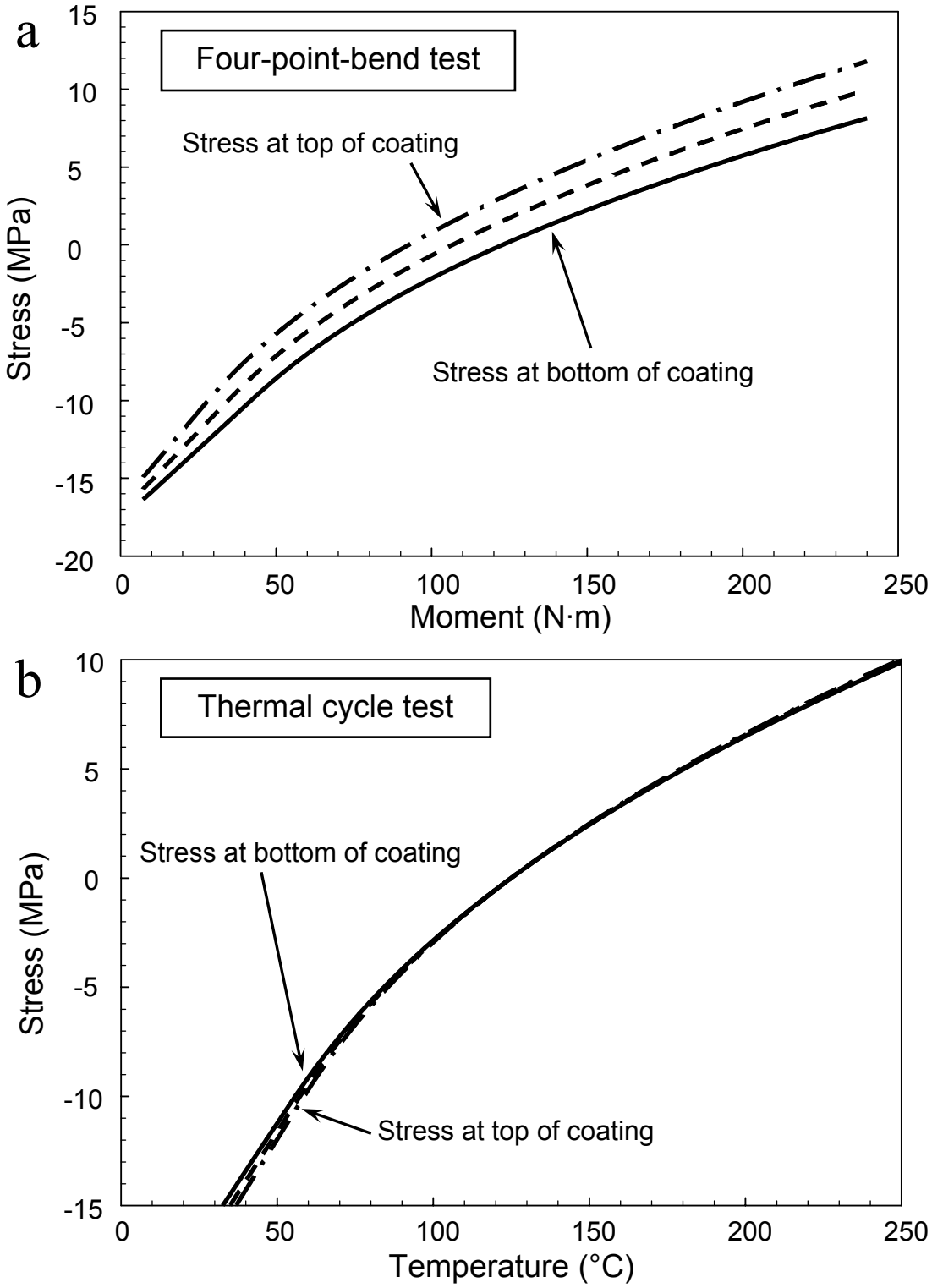

Figure 20. Axial stress variation at bottom, middle and top plane of coating. (a) As moment change under four-point-bend test, differences in stresses at different locations becomes larger. (b) There is barely difference between 3 planes within the coating as the temperature increases.

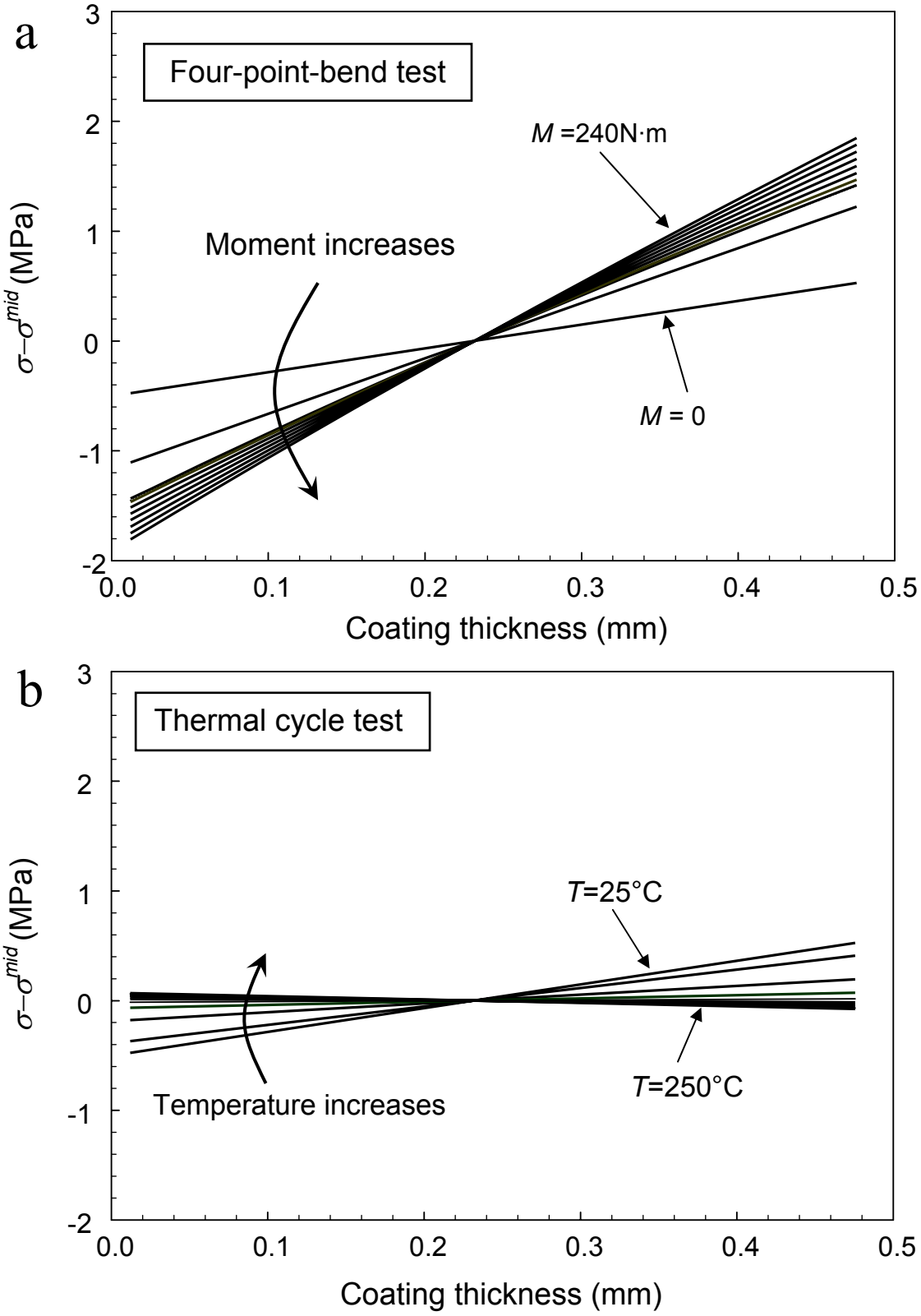

Figure 21. Axial stress difference between mid-plane and other positions through coating thickness. (a) Four-point-bend test. (b) Thermal cycle test.

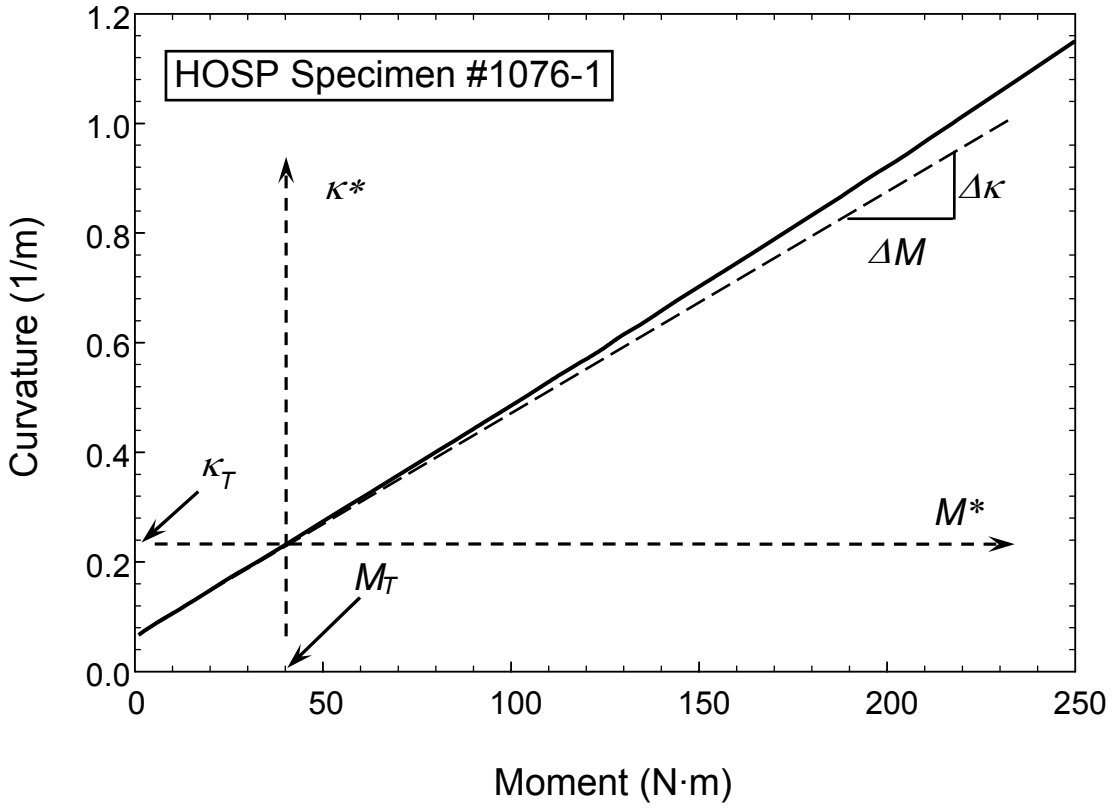

Figure 22. Moment-curvature relation of HOSP specimen under loading process. The transitional moment M_T and curvature κ_T are marked out. The slope of linear portion is used to calculate initial modulus. And the adjusted coordinate M^* - κ^* is presented.

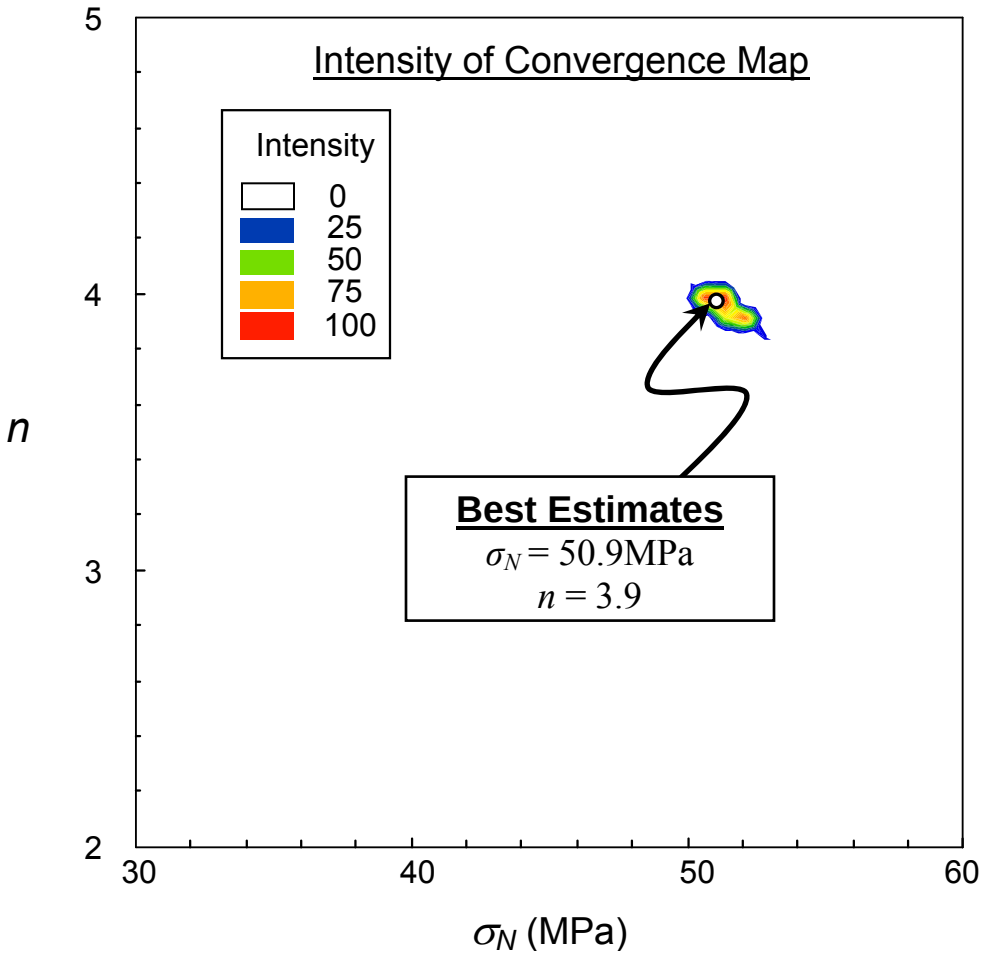

Figure 23. Intensity of convergence plot generated by the inverse analysis from measured curvature–temperature. The location of best estimates is determined from weighted averages of convergence.

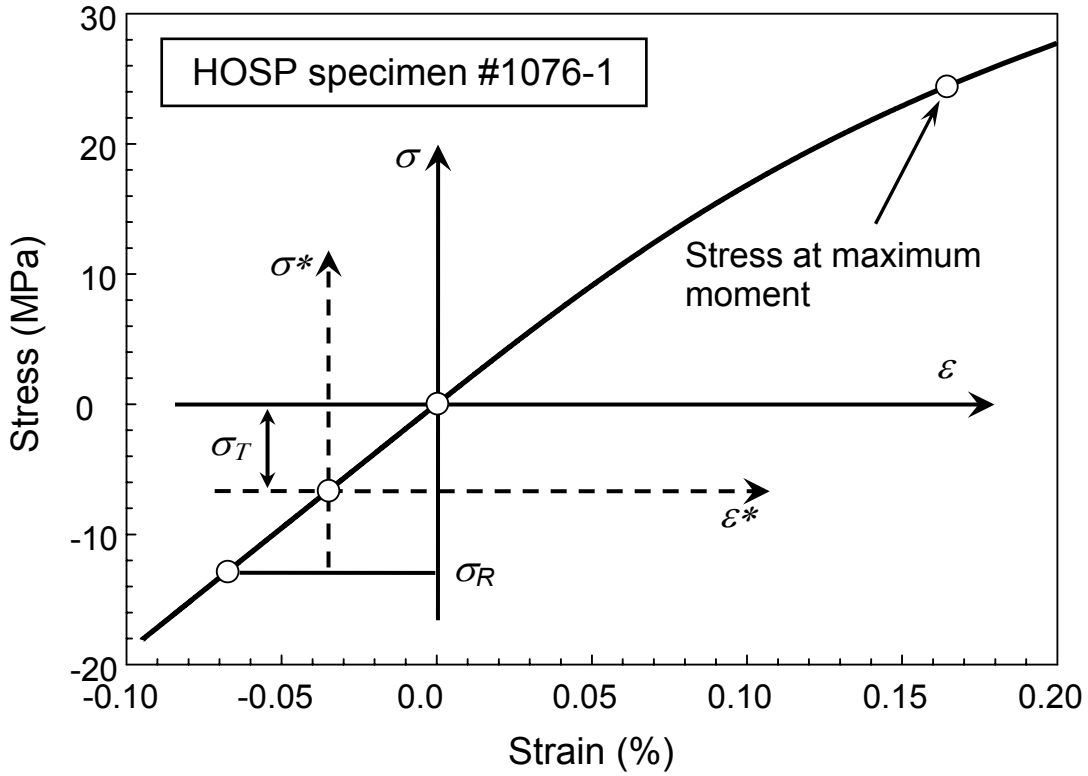

Figure 24. Nonlinear constitutive relation of TS YSZ coating estimated by the inverse analysis.

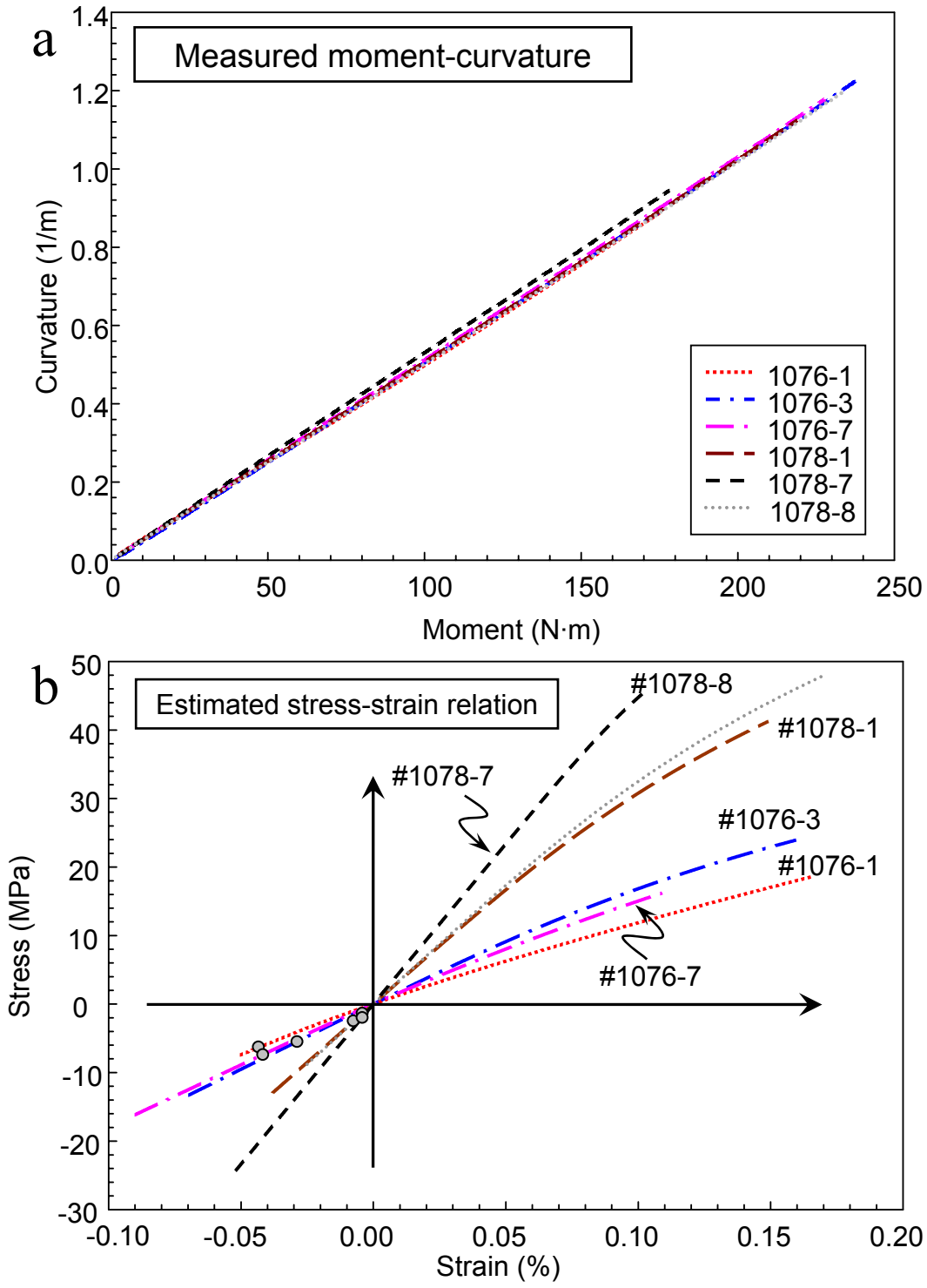

Figure 25. (a) Measured moment-curvature relations. Sample 1 and 3 are sprayed together along the direction perpendicular to the specimen length. Sample 7 is sprayed perpendicular to the length but reverse direction every time. Sample 8 is sprayed along the specimen length. (b) Estimated stress-strain relation under four-point-bend test for HOSP and FC specimens. Transitional points are marked out with gray dots.

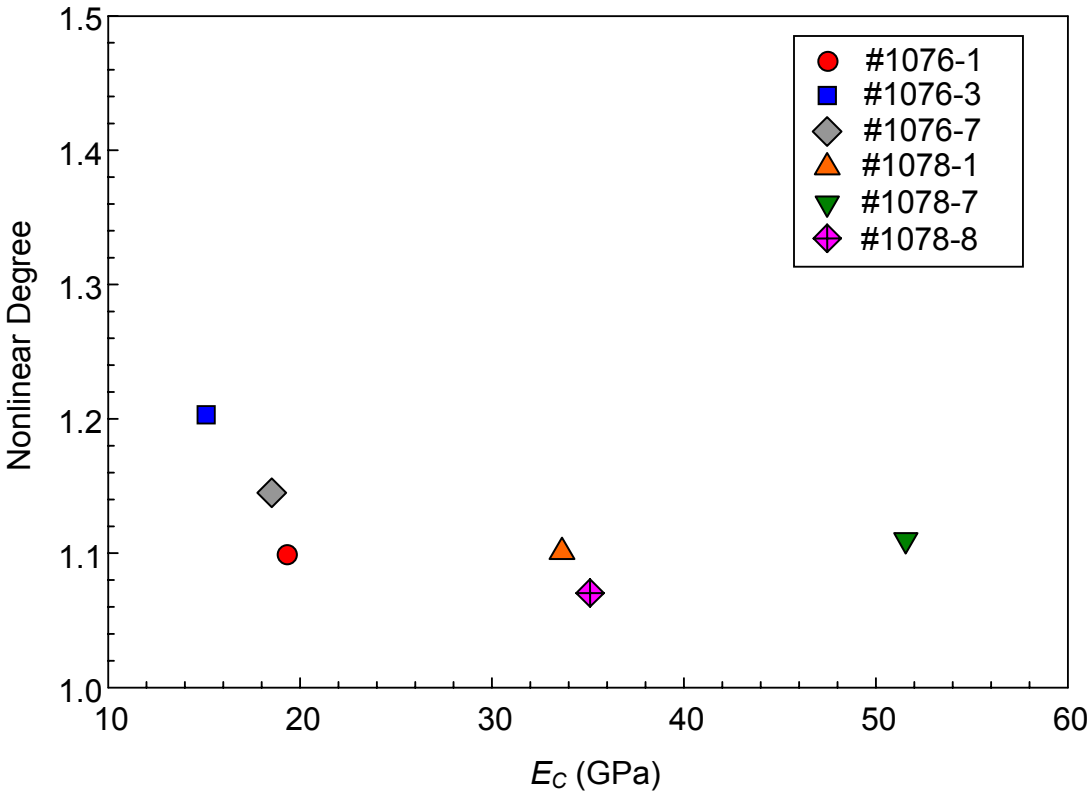

Figure 26. Elastic modulus-Nonlinear degree relation for YSZ coatings under four-point-bend test. FC specimens have slightly smaller nonlinear degree and much larger elastic modulus than HOSP specimens.

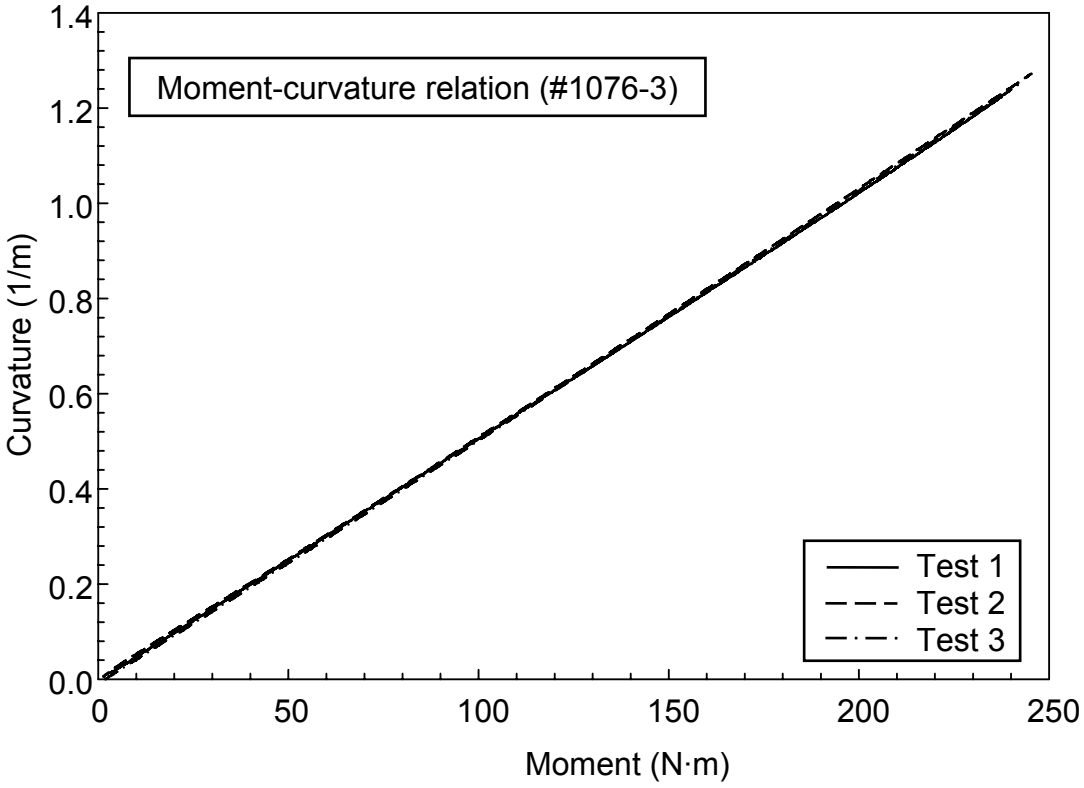

Figure 27. Measured moment-curvature relations for HOSP specimen #1076-3 from three separated tests. The similarity of three relations shows a good repeatability of four-point-bend test.

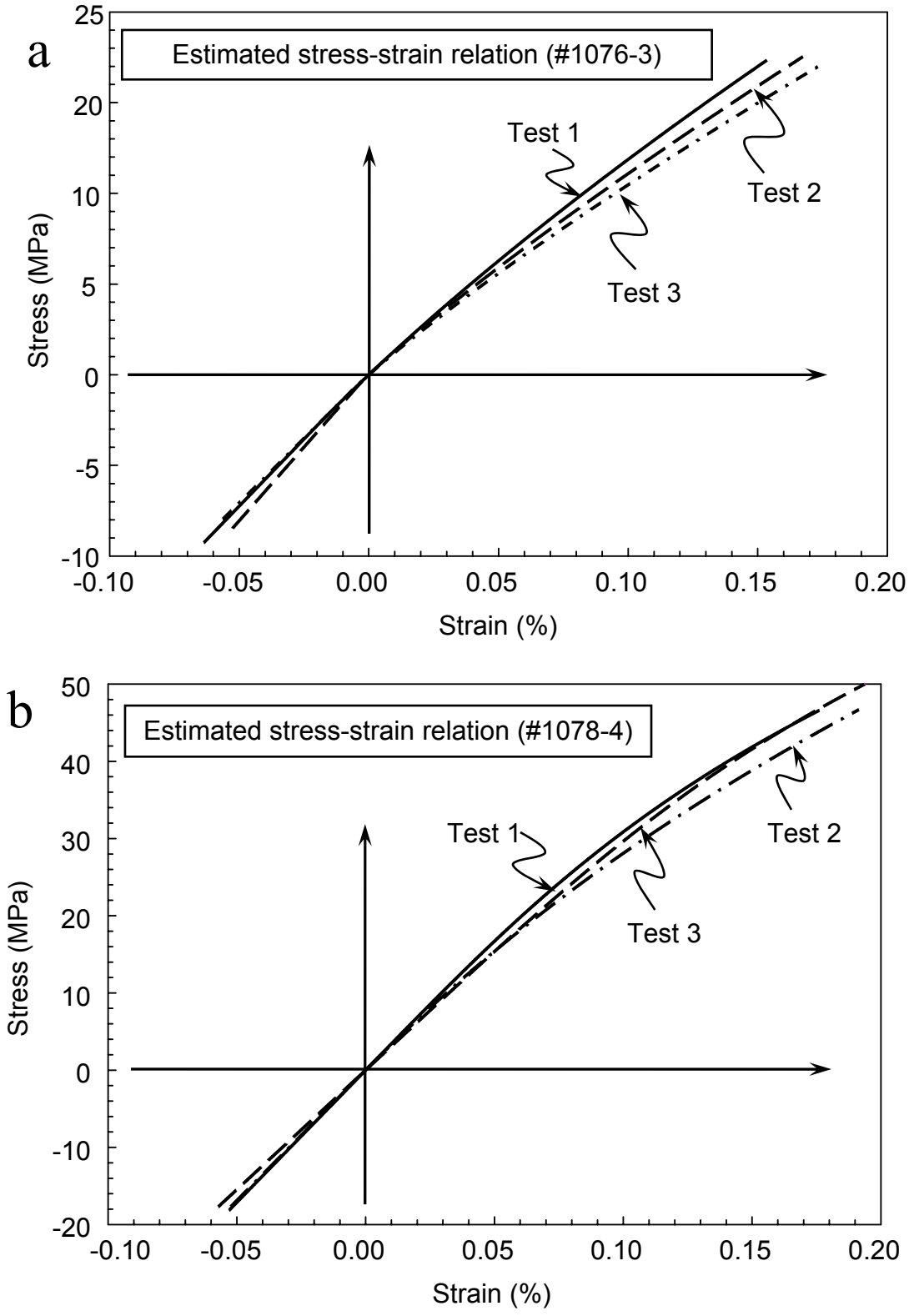

Figure 28. Repeatability test of four-point-bend procedure. The estimated stress-strain relations from separated tests show small differences. Specimens show softer behavior as the test number increases. (a) HOSP specimen #1076-3. (b) FC specimen #1078-4.

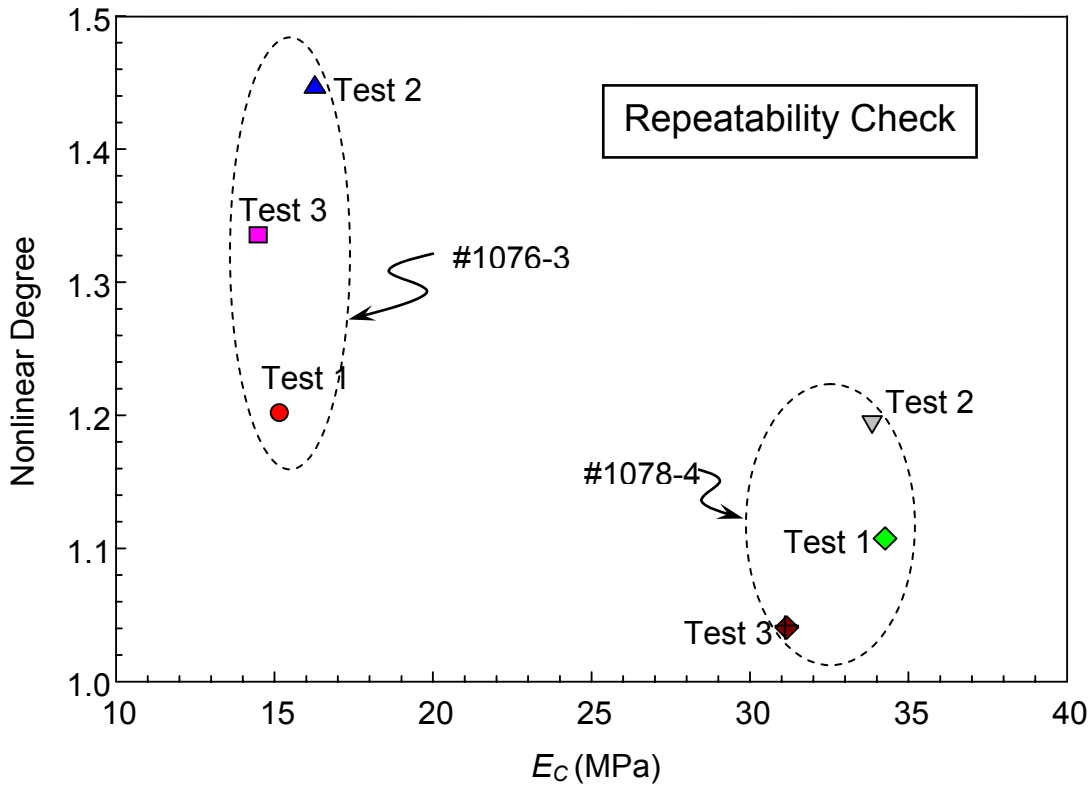

Figure 29. Repeatabilty check for HOSP #1076-3 and FC #1078-4. Elastic modulus of both spcimens shows a good repeatability, but nonlinear degree has small differences as the test number increases.

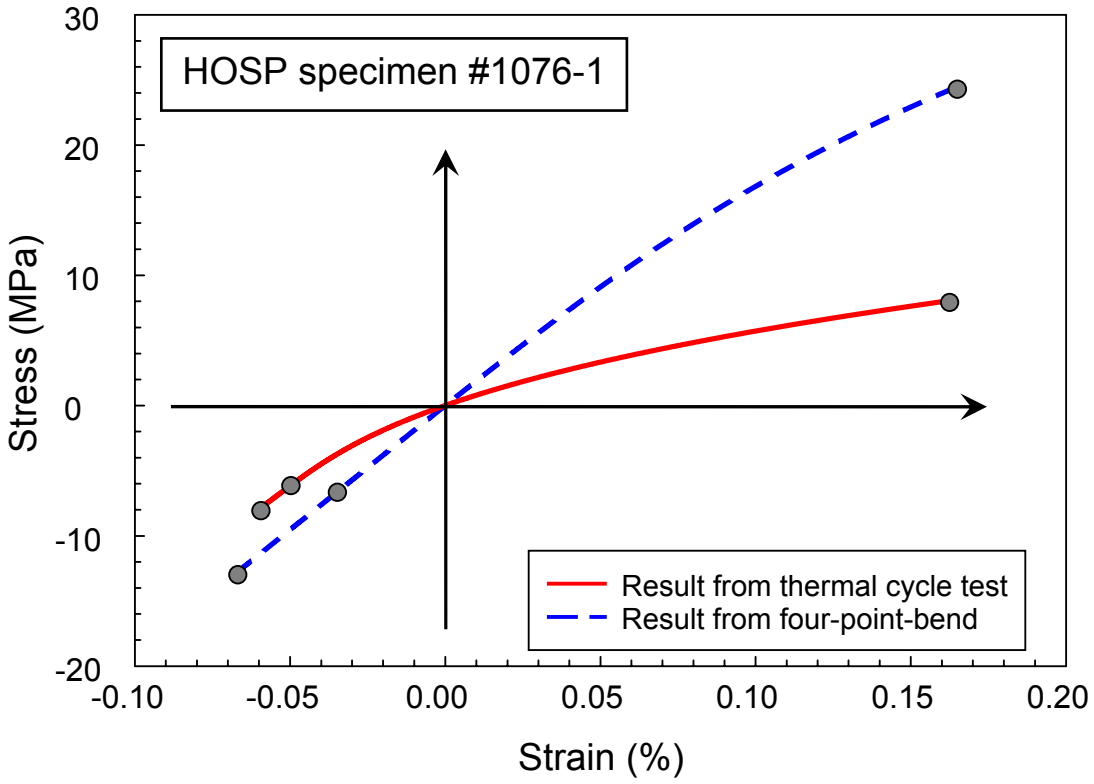

Figure 30. Comparison of the estimated stress-strain relation from four-point-bend test and thermal test. Transitional point, minimum stress and maximum stress are marked out with gray dots.

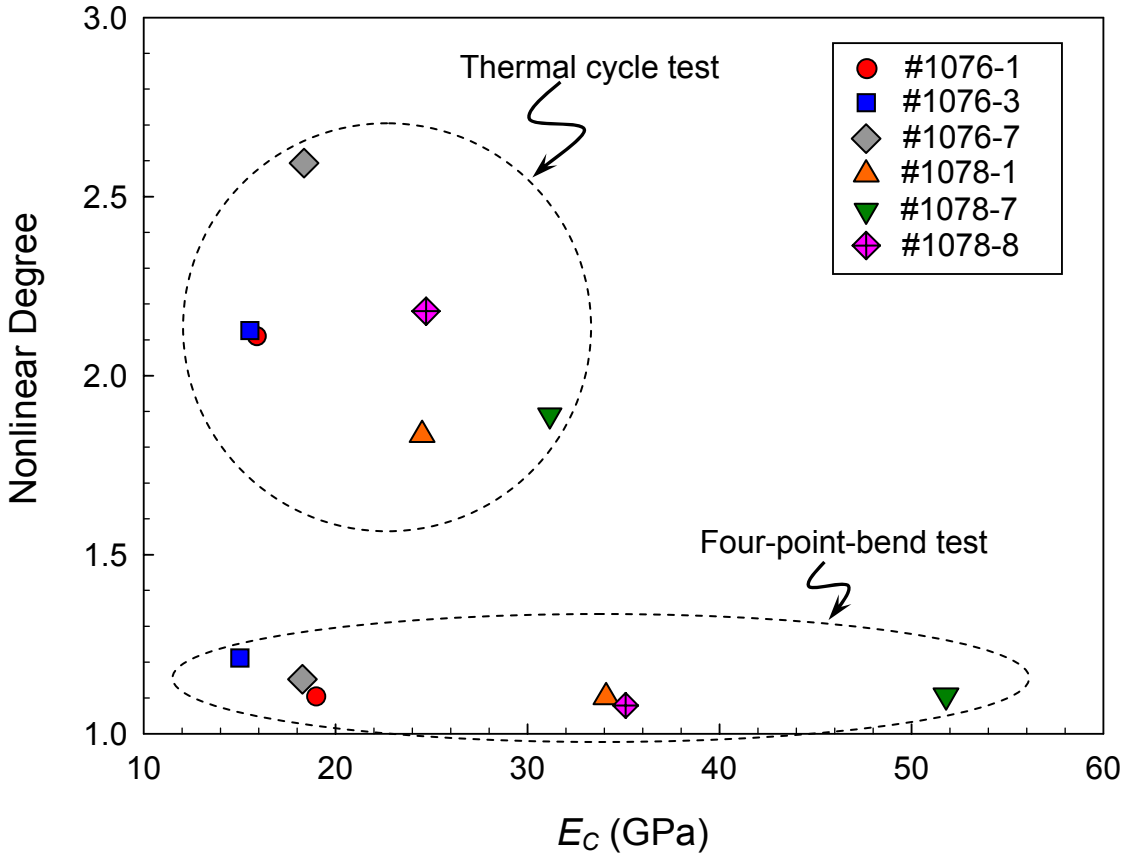

Figure 31. Comparison of nonlinear properties of HOSP and FC coatings under four-point-bend test and thermal cycle test.

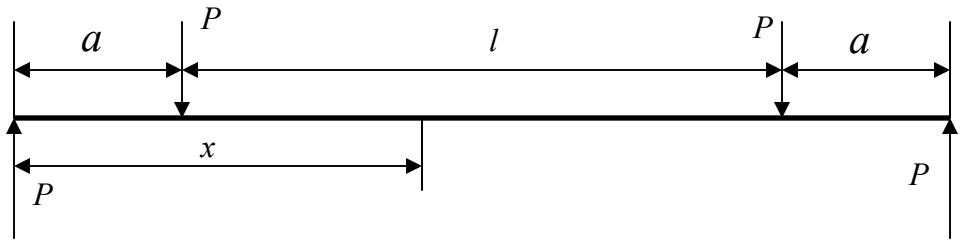

Figure 32. Schematic diagram of four-point-bend test. Inner span is *l*, and outer span is *a*. Under loading *P*, the deflection of the beam can be calculated.

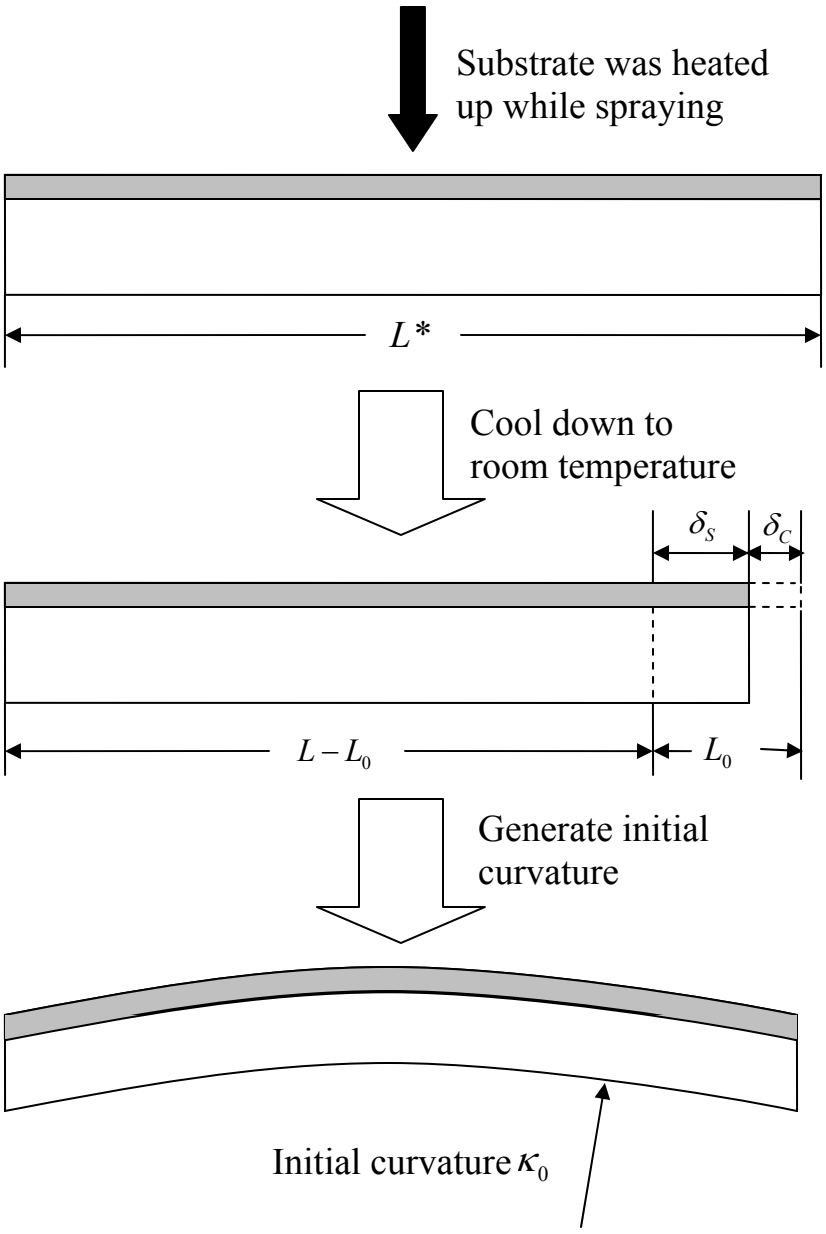

Figure 33. Approximate explanation of relation between the residual stress and the initial curvature. After the fabrication process, the mismatch in length of substrate and coating generated a mismatch force. Then the mismatch force can generate the initial curvature. The residual stress is considered as the combination of these two processes.

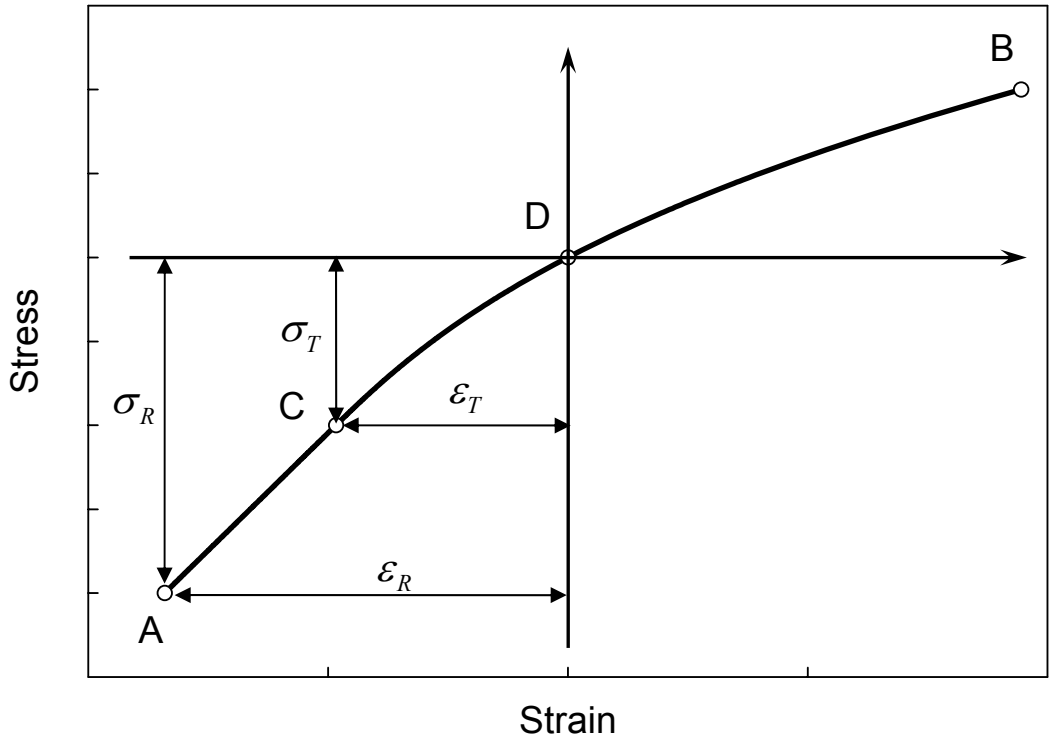

Figure 34. Typical nonlinear stress-strain relation of TS coating. Transitional point is *C*. Residual stress occurs at point *A*.

Table 1. Estimated unknown parameters and the errors between the input values.

Models		E_C (GPa)	σ_T (MPa)	σ_N (MPa)	n	σ_R (MPa)
1	Input	28	–10	20	3.5	–20
	Estimated (error)	26.3 (–5.9%)	–10.3 (3.9%)	19.3 (–3.4%)	3.56 (1.8%)	–20.1 (0.3%)
2	Input	50	–20	50	3.0	–28.6
	Estimated (error)	48.4 (–3.2%)	–20.1 (0.3%)	51.2 (2.3%)	3.42 (13.8%)	–28.6 (0.1%)
3	Input	40	–15	30	2.0	–20.5
	Estimated (error)	38.8 (–3.1%)	–15.0 (1.3%)	28.7 (–4.4%)	2.19 (9.3%)	–20.6 (0.5%)

Table 2. Estimated parameters corresponding to different transitional moment selected. Input parameters are: E_C = 28GPa, σ_T = –10MPa, σ_N = 30MPa, n = 2.5. And exact transitional moment is 50N·m

M_T (N·m) selected	E_C (GPa)	σ_T (MPa)	σ_N (MPa)	n
	Value (error)	Value (error)	Value (error)	Value (error)
40	27.9 (–0.3%)	–11.9 (19.3%)	32.1 (6.9%)	2.63 (5.1%)
50	27.9 (–0.1%)	–9.9 (–1.1%)	28.6 (–4.8%)	2.44 (2.5%)
60	27.8 (–0.5%)	–7.9 (21.1%)	25.2 (15.9%)	2.26 (9.5%)

Table 3a. Error analysis of calculation of initial modulus (four-point-bend test).

Parameters		*Ec* (GPa)
		Value (error)
t	No error	30
	+1%	29.6 (1.3%)
	−1%	30.4 (1.3%)
h	No error	30
	+1%	25.6 (14.7%)
	−1%	34.6 (15.2%)
Es	No error	30
	+1%	28.7 (4.4%)
	−1%	31.3 (4.4%)
$\Delta\kappa/\Delta M$	No error	30
	+1%	28.4 (5.3%)
	−1%	31.6 (5.5%)

Table 3b. Error analysis of calculation of initial modulus (thermal cycle test).

Parameters		*Ec* (GPa)
		Value (error)
t	No error	30
	+1%	29.6 (1.1%)
	−1%	30.4 (1.3%)
h	No error	30
	+1%	30.7 (2.4%)
	−1%	29.2 (2.4%)
Es	No error	30
	+1%	28.7 (4.4%)
	−1%	31.3 (4.4%)
$\Delta\kappa/\Delta T$	No error	30
	+1%	30.3 (1.3%)
	−1%	29.6 (1.3%)

Table 4a. Estimated parameters with artificial errors for material I (E_C = 31GPa, σ_T = –31MPa, σ_N = 51MPa, n = 3.23).

Estimated by Temp-curv relation with error bound ±0.002(1/m)							
	n	σ_N(MPa)	Convergence (0-10%/10%-15%)	Error	Ec(GPa)	σ_T (MPa)	Error
Original	3.15	51.4	98.5/1.5	2.8%	31	–31.5	1.7%
A	3.17	50.9	97.7/2.3	2.0%	31	–30.6	1.3%
B	3.17	51.2	97.2/2.8	2.0%	31	–32.5	4.9%
C	3.19	51.4	97.4/2.6	1.9%	31	–31.1	0.2%
D	3.18	51.2	95.7/4.3	1.9%	31	–32.6	3.4%
E	3.21	50.9	96.7/3.3	0.7%	31	–30.7	0.9%
average				1.7%		–31.4	2.2%
Estimated by Moment-curv relation with error bound ±0.0106(1/m)							
Original	3.22	49.5	95.3/4.7	5.0%	31	–31.6	2.0%
A	2.98	51.4	97.6/2.4	8.6%	31	–31.6	2.0%
B	3.43	48.3	81.6/10	11.3%	31	–31.6	2.0%
C	3.65	47.6	80.2/12.8	18.1%	31	–31.6	2.0%
D	3.33	48.4	98.9/1.1	9.2%	31	–31.6	2.0%
E	3.04	51.6	98.8/1.2	6.7%	31	–31.6	2.0%
average				10.8%		–31.6	2.0%

Table 4b. Estimated parameters with artificial errors for material II (E_C = 30GPa, σ_T = −11MPa, σ_N = 15MPa, n = 2.46).

Estimated by Temp-curv relation with error bound ±0.002(1/m)							
	n	σ_N(MPa)	Convergence(0-10%/10%-15%)	Error	Ec(GPa)	σ_T (MPa)	Error
Original	2.39	14.7	88.0/7.2	2.7%	30	−10.9	0.6%
A	2.44	14.8	87.6/2.6	0.9%	30	−10.9	0.1%
B	2.31	14.6	83.9/8.4	5.2%	30	−10.3	5.9%
C	2.36	14.9	94.7/5.2	3.5%	30	−10.1	8.4%
D	2.32	14.6	94.9/4.8	4.9%	30	−11.1	0.3%
E	2.36	14.7	85.4/5.5	2.6%	30	−11.3	2.7%
average				3.4%		−10.7	3.5%
Estimated by Moment-curv relation with error bound ±0.0106(1/m)							
Original	2.45	14.3	76.1/4.7	2.3%	30	−10.9	0.9%
A	2.36	14.1	76.4/9.1	4.6%	30	−10.9	0.9%
B	2.56	15.2	76.4/4.8	3.4%	30	−10.9	0.9%
C	2.48	13.9	90.7/5.8	3.6%	30	−10.9	0.9%
D	2.60	14.7	71.6/9.5	4.8%	30	−10.9	0.9%
E	2.58	15.5	89.6/7.0	4.4%	30	−10.9	0.9%
average				4.2%		−10.9	0.9%

Table 4c. Estimated parameters with artificial errors for material III (E_C = 23GPa, σ_T = −17MPa, σ_N = 29MPa, n = 2.88).

Estimated by Temp-curv relation with error bound ±0.002(1/m)							
	n	σ_N(MPa)	Convergence(0-10%/10%-15%)	Error	Ec(GPa)	σ_T (MPa)	Error
Original	2.78	29.2	92.5/5.1	3.3%	23	−17.1	0.5%
A	2.73	29.6	88.0/4.5	5.5%	23	−17.2	1.2%
B	2.78	29.3	92.6/5.6	3.6%	23	−17.4	2.5%
C	2.68	29.4	90.1/4.3	6.6%	23	−16.2	4.5%
D	2.68	29.5	90.1/4.1	6.9%	23	−17.6	4.0%
E	2.75	29.4	89.1/7.5	4.7%	23	−17.3	1.9%
average				5.5%		−17.2	2.7%
Estimated by Moment-curv relation with error bound ±0.0106(1/m)							
Original	2.79	28.3	95.5/4.1	4.0%	23	−17.0	0.0%
A	2.48	27.5	97.9/1.4	14.3%	23	−17.1	0.6%
B	3.27	27.9	73.8/11.7	13.7%	23	−17.1	0.6%
C	2.51	27.5	99.5/0.3	13.2%	23	−17.0	0.0%
D	2.78	28.3	97.7/2.0	4.1%	23	−17.0	0.0%
E	2.36	29.4	91.1/4.6	17.3%	23	−17.1	0.6%
average				12.5%		−17.1	0.4%

Table 5. Estimated parameters of HOSP and FC specimens from four-point-bend test.

Specimens		E_C (GPa)	σ_N (MPa)	n	σ_T (MPa)	σ_R (MPa)	ND
HOSP	#1076-1	19.1	50.9	3.96	–6.5	–13.1	1.098
	#1076-3	15.1	69.5	2.00	–1.8	–7.3	1.176
	#1076-7	18.3	79.4	2.37	–6.6	–16.3	1.167
FC	#1078-1	34.2	77.9	3.414	–0.3	–13.2	1.109
	#1078-7	46.8	71.5	8.011	–1	–26.9	1.044
	#1078-8	35.1	78.8	3.909	–0.46	–9.2	1.079

Table 6. Estimated parameters of HOSP and FC specimens from repeatbility tests

Specimens		E_C (GPa)	σ_N (MPa)	n	σ_T (MPa)	σ_R (MPa)	ND
HOSP #1076-3	Test 1	15.1	69.5	2.00	–1.8	–7.3	1.176
	Test 2	16.2	81.9	1.41	-0.6	-8.5	1.448
	Test 3	14.4	83.3	1.56	-1.3	-7.8	1.337
FC #1078-4	Test 1	34.2	78.0	3.41	-0.3	-13.7	1.109
	Test 2	33.8	108.6	2.24	-1.2	-12.6	1.196
	Test 3	31.1	113.8	3.39	-0.38	-12.3	1.042

Table 7. Estimated parameters of HOSP and FC specimens from thermal-cycle tests.

Specimens		E_C (GPa)	σ_N (MPa)	n	σ_T (MPa)	σ_R (MPa)	ND
HOSP	#1076-1	17.8	10.5	2.61	–6.2	–8.1	2.236
	#1076-3	17.2	8.4	2.19	–6.1	–8.2	2.429
	#1076-7	18.2	11.7	2.64	–14.5	–17.1	2.591
FC	#1078-1	27.3	21.3	1.80	–7.6	–14.4	1.938
	#1078-7	31.3	24.1	1.61	–16.2	–24.7	2.160
	#1078-8	23.3	17.8	2.25	–5.7	–9.9	1.883